INTERNSHIP REPORT:

Project supported by the attribution of a scholarship given by Paris Saclay University.

Investigation of Antarctic micrometeorites by the comparison with carbonaceous chondrites and cometary particles using Raman spectroscopy, infrared spectroscopy and mass spectrometry

Olivia Chitarra

Academic year 2017 – 2018

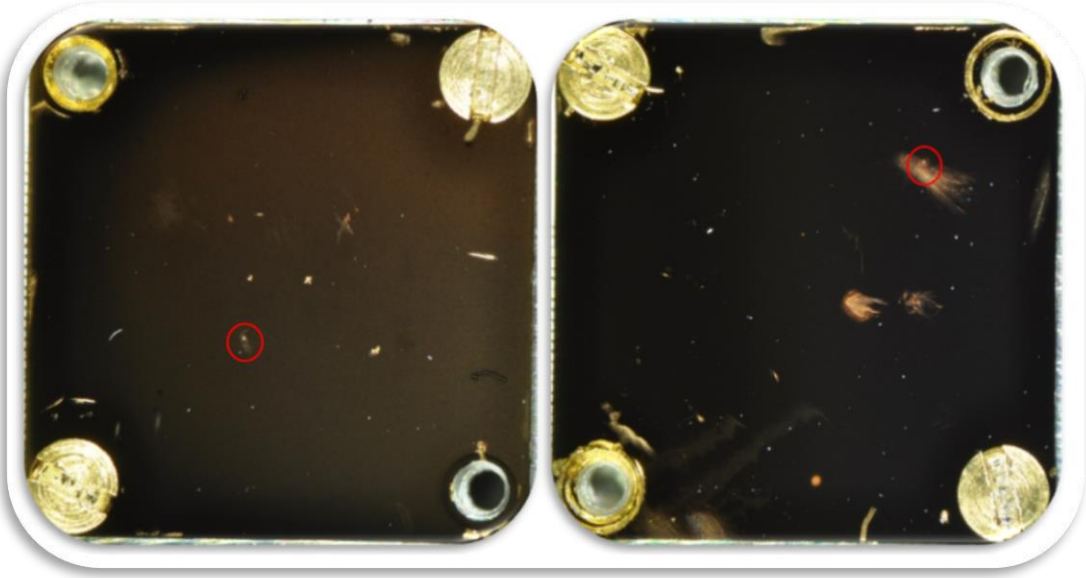

Optical images of the targets on which the two Antarctic Micrometeorites were deposited.

Under the direction of
Pr. Martin Hilchenbach
Dr. Sihane Merouane

ACKNOWLEDGMENTS

I would like to thank very especially Dr. Sihane Merouane for her incredible involvement with me. She has always been there to answer my questions, help, support and supervise me in a joyous and relaxed atmosphere. By her side, I have grown a lot as a scientist but also as a person.

I would also like to thank a lot Pr. Martin Hilchenbach for accepting me in his team, welcoming me and supervising me.

Then, I would like to thank my entire team: John Paquette and Oliver Stenzel for welcoming me and answering all my questions and for their supervision. Also, I would like to thank Stefanie Günther for her help for my adaptation and, as well, Susanne Kaufmann for the help she gave me with German and the administrative questions.

Furthermore, I would like to thank not only my colleagues but also the ones who became my friends: Sofia, Eliana, Paul-Louis, Amaury, Andrea, Sebastian, Fatima, Mahmood, Sudarshan, Mariangela, Mayukh, Ramada and Sihane. They made this experience more enriching than I could ever had hoped.

Moreover, I would like to thank the Max Planck Institute for welcoming me and all the members of the institute who created a joyful atmosphere during these four months of internship.

Finally, I would like to thank the Paris Saclay University for the scholarship they granted me as well as Donia Baklouti for the help for finding this internship.

TABLE OF CONTENTS

1 INTRODUCTION

1.1 Extraterrestrial materials

4.56 billion years ago, the molecular cloud from which the Sun was born collapsed, giving birth to the Sun surrounded by a disk of dust and gas: the protoplanetary disk. In this disk, dust grains formed and collided with each other thus accreting to form larger and larger objects. When objects reached the size of a planet, the energy from short-lived radionuclides and, to a lesser extent, the energy accumulated from the accretion, lead to heating and differentiation. During this process, heavy elements migrated to the center of the object while light elements concentrated at its surface. Hence, these objects have lost their primitive composition.

However, some bodies were small enough to not differentiate, they are known today as asteroids and comets. Most of the known asteroids are located in the Main Belt, between Mars and Jupiter, thus inside the snow line. Therefore, most of them may have lost volatiles they could contain and have experienced significant thermal alteration. Comets, on the other hand, are of particular interest as they formed far from the Sun, in the external regions of the protosolar nebula and remained beyond the snow line most of their lifetime. Hence, they have been able to retain volatile species and eventually presolar material (Willacy et al., 2015). The study of cometary material is thus of major interest for the study of the early stages of the Solar System.

1.1.1 Comets

Comets are considered as the most primitive objects of our solar system. Therefore, they are studied in two main science fields: planetary science and astrobiology.

Comets are made of the most primitive materials and the study of their composition can allow the access to information about physico-chemical conditions and processes that lead to the formation of planets (Caselli and Ceccarelli 2012).

Furthermore, comets consist of ices, inorganic and complex organic molecules. Since the early Earth has been bombarded by small bodies, comets could have played a key role in the delivery of water and organic material essential for the apparition of life (Cottin et al. 2015; Oro 1961).

Comets are small bodies of the solar system in orbit around the Sun with short or long period. They are made of a mixture of ices and dust. When comets get close to the Sun, the ices sublimate, releasing gas and dust. This phenomenon is at the origin of the comet dust tail that is observable when comets are active.

1.1.2 Meteorites

Meteorites are celestial bodies that reach the Earth surface. Therefore, they present an opportunity to analyze Solar System bodies in the laboratory.

Meteorites can be classified based on their composition and can be separated into two groups: differentiated and undifferentiated meteorites (F. Brandstätter, 2012). The differentiated meteorites come from differentiated parent bodies like planets, large asteroids or satellites. The undifferentiated meteorites, also called chondrites (the meteorites studied in this work) come from undifferentiated parents bodies and contain chondrules (small spherical silicate inclusions). Among the chondrite meteorites, I will focus on carbonaceous chondrites, the most primitive meteorites. This group contains eight different sub-groups of carbonaceous chondrites (CI, CO, CV, CR, CK, CH and CB) which can be distinguished by the degree of aqueous alteration and thermal metamorphism. In particular, CI type chondrites are used as a reference for comparing the chemical composition of other celestial samples because their elemental composition is close to the composition of the photosphere (Ringwood et al., 1979)

These meteorites are made of mineral and organic phases. The organic phase is divided into the Soluble Organic Matter (SOM), which contains compounds soluble in classic solvents (water, ethanol, acetone…) and the Insoluble Organic Matter (IOM) which is made of a complex macromolecular material (Sephton et al., 2002 and references therein).

1.1.3 Micrometeorites

Celestial bodies are collected after their fall on the Earth surface. However, there are other ways to collect celestial dust. It is possible to get them in the stratosphere (Interplanetary Dust Particles, IDPs) but also in very specific regions of the planet. For example, some dust particles are retrieved in the Antarctic region (Maurette et al., 1991) because it is considered a clean environment thanks to the low human activity, the remoteness from the coasts and the cold and dry weather. The micrometeorites are trapped in the snow and, therefore, preserved from mechanical, biological or aqueous alteration.

1.2 The Rosetta mission to comet 67P/ Churyumov-Gerasimenko

1.2.1 Previous mission

The first mission to conduct *in situ* measurements of a comet was Giotto, which encountered comet Halley in 1986. In total, six different comets have been visited during twelve different spatial missions. In 2004, comet Wild 2 has been visited by the Stardust spacecraft which brought back to Earth in 2006 the first cometary samples (Brownlee et al., 2006).

1.2.2 The Rosetta mission

In 2014 (August, 6), after a ten years journey, the Rosetta spacecraft reached the comet 67P/ Churyumov-Gerasimenko. In total, twenty-one different instruments were on-board the Rosetta orbiter and the lander Philae. The COSIMA (COmetary Secondary Ions Mass Analyzer) instrument on board the orbiter was conceived in order to study *in situ* the refractory material of the comet, or in other words, the chemical composition of solid particles ejected from the comet.

This study was important because the previous collection of dust particles by the Stardust mission was done with a high impact velocity (around 6.1 km. s^{-1}). Because of that speed, many particles melted or exploded upon impact in the collector. Therefore, only the very refractory materials (that can tolerate high temperature) could be analyzed. In the case of COSIMA, the particles were collected at low impact velocity (less than 10 $m.s^{-1}$). Therefore, the chemical and the mineral composition have been better preserved which allow a better quantification and general study of the material (Hilchenbach et al., 2016)

1.3 Goal of this study

The origin of given Antarctic Micrometeorites (AMMs) is unknown. They are thought to come from small bodies of the Solar System, but they could originate from both asteroids and comets. The main aim of this study is to analyze two different and unknown AMMs and to compare them with the dust particles from 67P and to five different carbonaceous chondrites. The goal is to be able to classify them among extraterrestrial material families.

In order to do so, three different techniques have been used on these samples (Günther et al., 2017): Raman spectroscopy, electron microscopy with energy dispersive X-Ray spectroscopy (SEM-EDX) and time-of-flight secondary ion mass spectrometry (ToF-SIMS).
Thereby, my work has consisted of:

- Performing complementary Raman measurements on carbonaceous chondrites.
- Processing the ToF-SIMS data in order to get the elemental composition of the samples.
- Process and analyzing Raman and Infrared data in order to give a precise mineralogical composition of the samples.
- Comparing the results from all the techniques to speculate on the potential origin of the studied AMMs.

In the section 2, I will present all the techniques (the instruments as well as the theories behind them) and the samples that I used. In the section 3, I will describe the data processing. I will present the results in section 4 and they will finally be discussed in the section 5.

2 MATERIALS AND THEORY

In this chapter, I will present all the instruments and techniques, but also the samples that I used during the internship.

2.1 Sample preparation

The sample preparation was done before my arrival, my internship being focused on the analyses of spectroscopic data. However, I will introduce the samples I have worked with by briefly describing in this section how they have been prepared.

2.1.1 Antarctic micrometeorites

The two micrometeorites studied here have been collected in the Antarctic snow near the Concordia Research Station. In order to extract them, the snow has been melted and the Antarctic Micrometeorites (AMMs) have been retrieved with a sieve. Then, they have been stored for 12 years between two microscope-glass slides and kept in a clean environment.

The two AMMs were placed on gold targets (1cm x 1cm) previously covered by a nanopowder of gold obtained by evaporation of gold at low pressure (see figure 2.1). The transfer to each target was different for the two particles. For the sample DC 06-07-54-07 (hereafter AMM7), a brush wetted with water was used. For the sample DC 06-07-162 (AMM162), a brush wetted with ethanol was used. Concerning the size of the two particles, AMM7 has a size of 38 µm x 67µm x 32µm and AMM162 has a size of 23µm x 20µm x 29µm.

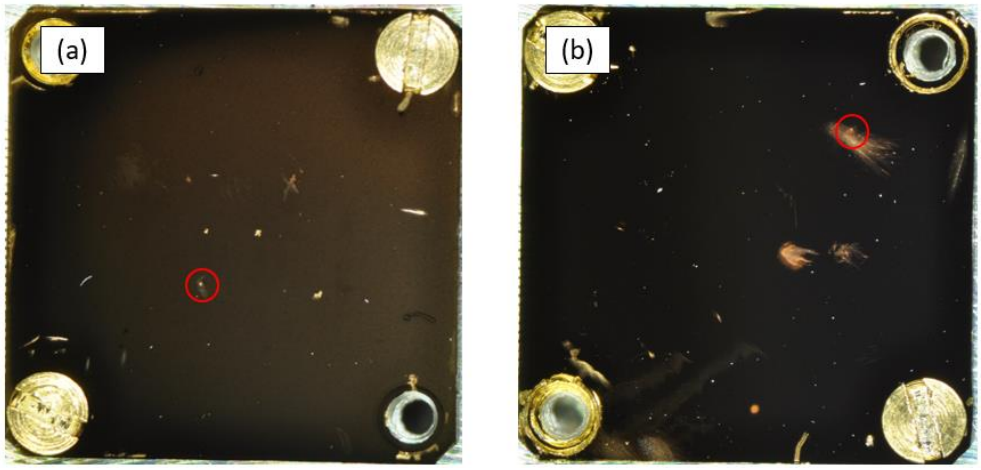

Figure 2.1: optical images of the two targets on which (a) the AMM7 and (b) the AMM162 were deposited. The red circles show the locations of each AMM.

2.1.2 Carbonaceous chondrites

In addition of the two Antarctic micrometeorites, I also studied five different meteorites (all are carbonaceous chondrites): Murchison (CM), Orgueil (CI), Renazzo (CR), Lancé (CO) and Allende (CV). Fragments from these meteorites were transferred on a clean gold target (1cm x 1cm) with a Ti tweezer. They were pressed on the gold foil in a micropress with a sapphire window. The optical image of the target is shown in figure 2.2.

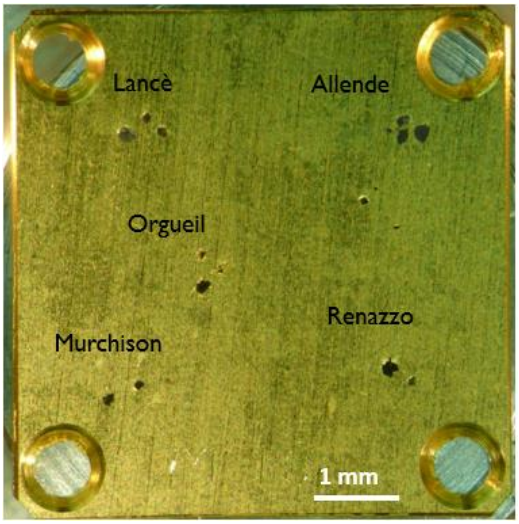

Figure 2.2: optical image of the gold target with all meteorite fragments.

2.2 Raman spectroscopy

2.2.1 Principle of Raman spectroscopy

The Raman spectroscopy is based on the sample excitation by a laser. If the incident photons have the same energy as a vibration level of the sample, there is an absorption phenomenon which is the principle of the infrared spectroscopy (see next section). However, if the incident photons have a higher energy than a vibration level, there is a scattering phenomenon (see figure 2.3):

- If the incident and scattered photons have the same energy, it is Rayleigh scattering
- If the scattered photons have a lower (or higher) energy than the incident photons, it is Raman Stokes (or anti-Stokes) scattering

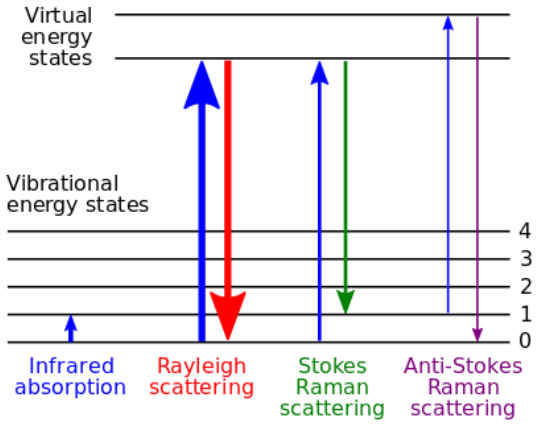

Figure 2.3: explanation of the Raman principle.

This technique, which is non-destructive for the sample as long as the power of the laser is kept low, allows the identification of many minerals and the detection of organic materials. However, some mineral signals can overlap with each other which makes the identification difficult. Furthermore, fluorescence phenomena can also occurs and can prevent the analysis as it leads to an increase of the spectral baseline that masks the features that could be present.

2.2.2 Instrumentation

I performed the Raman measurement using a Witec Alpha 3000 Raman Spectroscope with x50 and x100 objectives and a laser with a wavelength of 532 nm (see figure 2.4)

The spectrograph calibration was checked using a calcite reference sample (more details are given in the method section). In order to protect potential organic material, I used a low laser power between 2 and 3 mW.

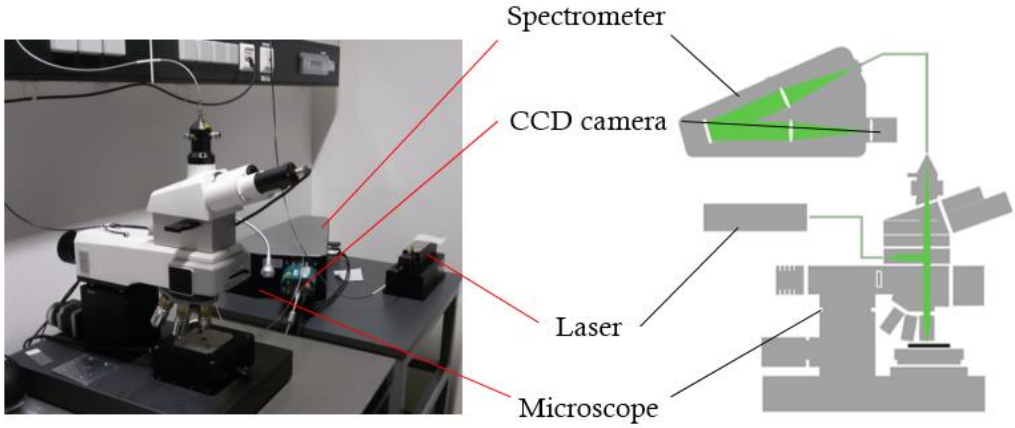

Figure 2.4: picture (left) and sketch (right) of the Raman instrument used.

2.3 Infrared spectroscopy

During my internship, I had the possibility to also work on infrared data because infrared spectra have been taken on a Murchison sample (described in Stenzel et al., 2017), just before my arrival at the MPS.

2.3.1 Principle of IR spectroscopy

If an incident photon (whose energy is in the infrared range) is absorbed by the sample, it means that the photon has the same energy as a vibration-rotation level. Therefore, each compound will have its own signature (according to the bond geometry, vibration or rotation type and if the ro-vibration is active or not).

Furthermore, in the case of the mid-infrared (from 3997.5 cm^{-1} to 599.7 cm^{-1} i.e. from 2.5 µm to 16.7 µm), it is possible to observe signals from minerals because the fundamental molecular vibration bands of a lot of rock-forming minerals are located in the mid-infrared. It is possible, for minerals, to observe different spectral features at different spectral ranges (Salisbury et al., 1993). In this case, we have three different behaviors (which are illustrated using one spectrum from our dataset in figure 2.5):

The Reststrahlen bands

The Reststrahlen bands are due to a surface scattering. At low wavenumber (i.e. high wavelength), the material reacts like a mirror. It is called the first surface reflection because all incident photons are reflected from the surface of the sample. Therefore, we observe reflectance bands (the blue trace in figure 2.5). There are called Reststrahlen bands because we actually observe rays left after such a reflectance (residual rays). In the case of meteorites, this feature tends to be subtle.

The Absorption bands

These bands (black part in the figure 2.5) are due to the volume scattering. In this wavenumber region, absorption coefficients are low and this can lead to volume scattering. In the case of meteorites, and as we can see in the figure 2.5, the absorption bands dominate the spectrum.

The Christiansen feature

This phenomenon takes place in a wavelength range in which a quick change occurs for the real part of the refractive index of the sample and, therefore, it can become close to the medium refractive index of the surrounding medium (air in this case). The position of the Christiansen feature (marked with the red arrow in the figure 2.5) can vary according to the nature of the sample and also to the type of the meteorite (around 1100 cm^{-1} for carbonaceous chondrites).

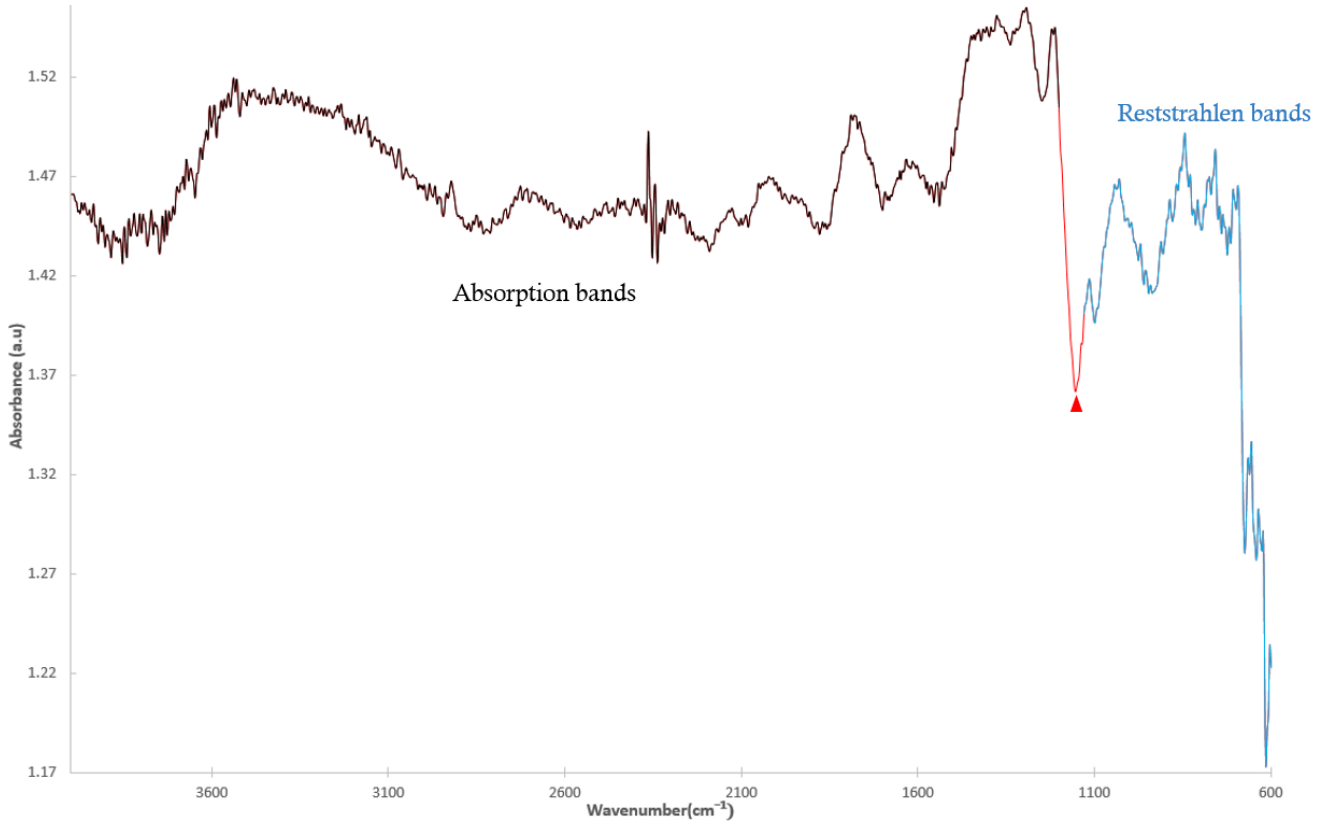

Figure 2.5: infrared spectrum of a carbonaceous chondrite with different features: absorption bands (black), reststrahlen bands (blue) and Christiansen feature (red arrow).

2.3.2 Instrumentation

These spectra have been measured by Barbara Stefke and colleagues at the University of Natural Resources and Life Sciences in Vienna (Austria). They used an IR-Microscope Bruker Hyperion 2000 (FTIR) and they used a quadratic measuring spot (70 µm x 70 µm). The range of the measurement was from 3997.5 cm^{-1} to 599.7 cm^{-1} (i.e. from 2.5 µm to 16.7 µm).

2.4 ToF-SIMS spectroscopy

2.4.1 The principle of ToF-SIMS

The Time-of-flight (TOF) is based on the speed difference of secondary ions. The primary ion beam hits the particle and secondary ions are sputtered from its surface. Then, they are accelerated thanks to the application of an electric field in order to hit the detector after flying through a time-of-flight tube. Ions with the same charges will acquire the same kinetic energy. However, the speed of the secondary ions depends on the mass to charge ratio. Therefore, the time to get to the detector is measured and connected to the mass to charge ratio.

It is possible to collect either the positive secondary ions, either the negative secondary ions. In this work, I will only focus on positive spectra from which we can derive the abundances of most of the rock forming elements.

2.4.2 Instrumentation

On board the Rosetta spacecraft, there is a time of flight secondary ion mass spectrometer, COSIMA (COmetary Secondary Ion Mass Analyser) which acquired mass spectra in situ on cometary dust particles collected in the inner coma of the comet 67P until September 2016 (Kissel et al, 2007; Hilchenbach et al., 2016). A schematic model of the instrument is shown in figure 2.6. In order to be able to do a direct comparison of samples measured in the laboratory with the flight data, there is a reference model of COSIMA (which is a replica of the flight instrument) located in the Max Planck Institute for Solar System Research in Göttingen (Germany). All the ToF-SIMS data of the AMMs and meteorites I have worked with have been acquired with the reference model. The primary ion beam is composed of positive indium ions accelerated to 8 keV. The spot on the sample is an ellipse of about 35 µm x 50 µm.

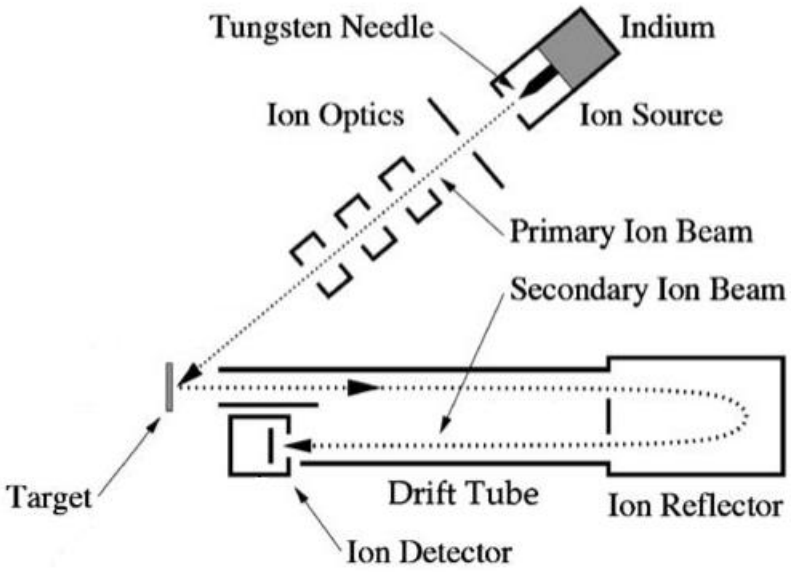

Figure 2.6: schematic view of the COSIMA instrument (Kissel et al., 2007)

3 METHODS

3.1 ToF-SIMS spectra

3.1.1 Selection of the ON and OFF particles data

Spectra have been measured for each sample. I decided to study the samples that have been also measured with other analytical techniques in order to be able to do a direct comparison between these techniques. Unfortunately, it was not possible for the Orgueil meteorite because the fragment analyzed in Raman was too small to be measured with the ToF-SIMS technique. For this sample only, I decided to use another fragment.

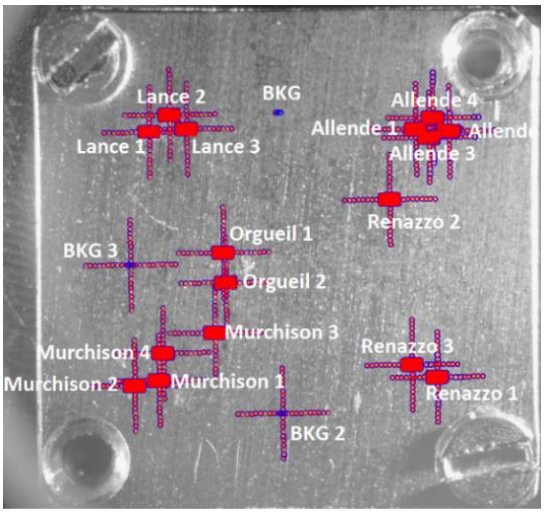

Figure 3.1: picture of the target with our five meteorites. Each red and blue circle represents the position at which a positive and a negative mass spectrum has been acquired, respectively.

As we can see on the figure 3.1, spectra in the positive mode (red circles in figure 3.1) and the negative mode (blue circles in figure 3.1) have been taken on each sample. Because the target contains terrestrial contamination, it is important to account for it when measuring the composition of the samples. Thus, spectra were also taken on the background in the vicinity of the samples. That will allow me to always compare spectra measured on the meteorite (or the AMMs) with spectra measured on the background.

Therefore, the first step is to select which spectra have been taken ON and OFF the samples. In order to do so, for each spectrum (corresponding to one position in the x and y axis), I extract the counts values for elements that are expected to be found in the particles (such as Mg or Na) or on the background (such as Au or PDMS). PDMS (or PolyDiMethylSiloxane) is the main source of contamination on the target.

Hence, it is possible to plot ion counts as a function of the position (on the x and y axis) as illustrated in figure 3.2. In this case, I chose the magnesium (m/z = 23.99) as the representative of the particle and the PDMS fragment $Si(CH_3)_3^+$ (m/z = 73.05) as the representative of the background. The selection of ON and OFF the particle is made by looking for regions where both the PDMS is low and the Mg is high. Figure 3.2 shows an example of such a spectra selection.

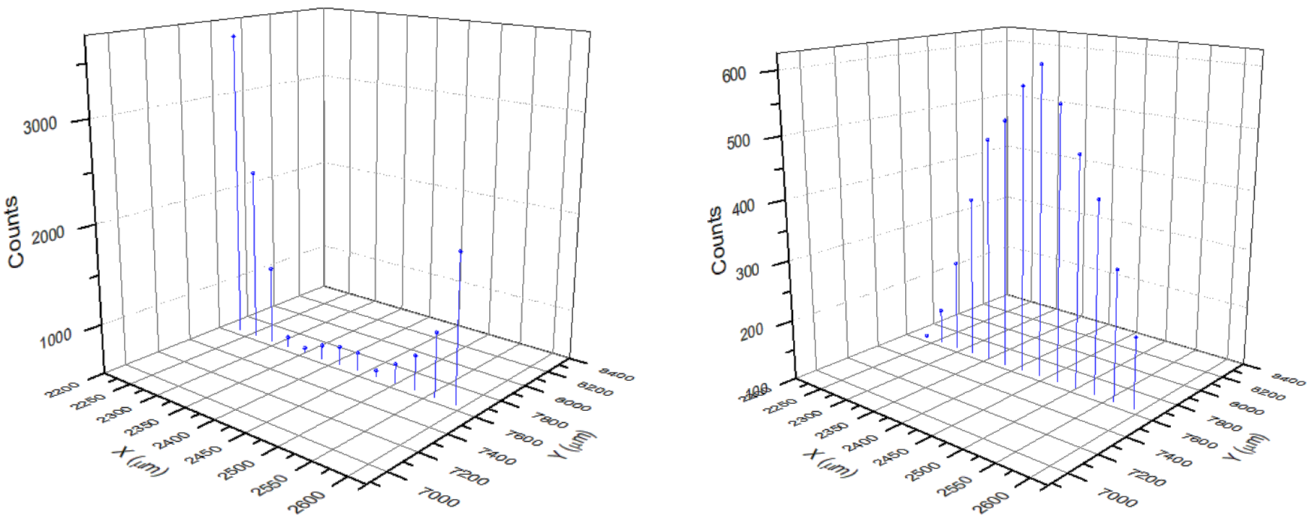

Figure 3.2: spatial distribution of the PDMS intensity (on the left side) and of the Mg intensity (on the right side) for the particle Lancé. The PDMS intensity will be high OFF the particle and low ON the particle (and it is be the opposite for the Mg intensity). By using this method, it is possible to know which spectra are located on the particle and which ones are located on the background (see **figure 3.3**).

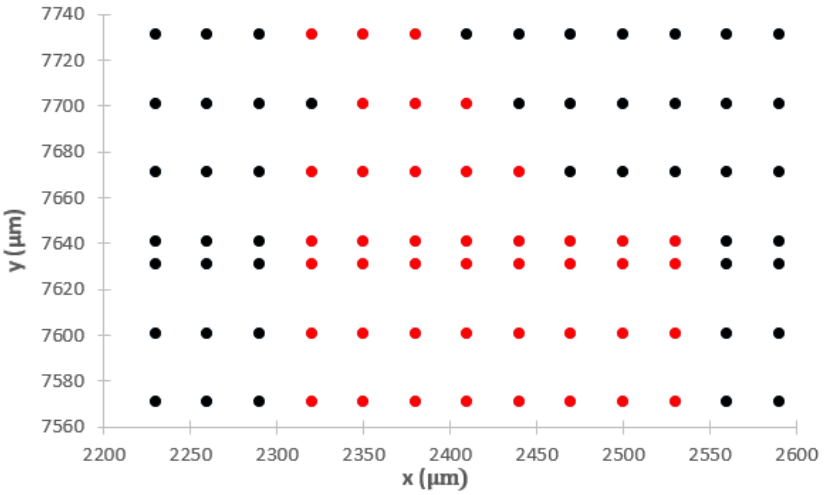

Figure 3.3: selection of the ON (red dots) and OFF (black dots) spectra along the x and the y axes for the Lancé sample.

3.1.2 Fitting procedure

Once we know which spectra are ON the particle and which ones are OFF and before any calculation, every spectrum is mass calibrated using the pipeline developed by John Paquette and Oliver Stenzel. The pipeline also allows us to fit every peak present in the spectra by up to four Gaussian curves and provides, at each m/z, the width, the position and the number of counts of these fitted Gaussians. In order to increase the signal to noise ratio and so to allow the detection of elements with a low signal, every spectrum selected as ON (and OFF) the particle are summed together to create a spectrum ON- and a spectrum OFF. The fits are then performed on these summed spectra.

3.1.3 Data analysis

In order to subtract the contribution of the terrestrial contamination, the first step is to normalize all the spectra. To do so, I decided to normalize to the PDMS peak intensity. There are three major reasons for this choice. First of all, PDMS is the main contributor of the background and the peak at m/z = 73.05 is the highest one. Moreover, we know that meteorites and comets consist of silicate minerals (Günther et al., 2017) and of organic compounds (Fray et al., 2016). Hence, C and Si are two important elements that we find in the PDMS contamination. It is therefore important to know the PDMS contribution as precisely as possible in order to obtain the best abundance estimation possible for C and Si. Finally, we don't expect to find such compound in either meteorites or micrometeorites thus the signal we measure is expected to come only from the contamination.

Therefore, for every particle with their set of ON and OFF spectra, I determine the counts value of the PDMS peak at m/z = 73.05 (hereafter I^{ON}_{PDMS} for spectra ON the particle and I^{OFF}_{PDMS} for spectra OFF the particle). Thus, the peak intensity of the particle, I (spectra ON after normalization) is given as follows:

$$I'_E = I^{ON}_E \times \left(\frac{I^{OFF}_{PDMS}}{I^{ON}_{PDMS}}\right)$$

Here, I^{ON}_E correspond to the peak intensity of the element E for the particle before the normalization.
Moreover, the symbol '' ′ '' denotes intensity after normalization (and the absence of this symbol denotes intensity before the normalization).

3.1.4 Elemental composition of the samples

The main aim of the mass study is the quantification of secondary ions via the determination of relative abundances. Hence, the relative quantification of an element depends on the ion intensity of the reference element (in our case Fe except for the quantification of C for which I had to use Si as the reference element) in the mass spectrum and on a relative sensitivity factor (RSF) coming from a standard calibration and defined as follows (Bardyn, 2016):

$$RSF\,(E, E_0) = \frac{\left(\frac{E^+}{{E_0}^+}\right)_{standard}}{\left(\frac{E}{E_0}\right)_{standard}}$$

E is the element for which we want to derive the abundance, E_0 is the reference element, E^+ and E_0^+ are the secondary ions intensities of those elements and E/E_0 is the actual elemental ratio of the standard. It is, therefore, important to choose the standard carefully. In this case, I choose to use the RSF already used to measure the elemental abundance for the comet 67P (Bardyn et al., 2017) which allows me to do a direct comparison of the results. The only difference is for the element O because this element was quantified using the negative spectra in Bardyn et al., 2017. In this work, I only used positive spectra. Thus, for this element only, I used the RSF given in Krüger et al., 2015.

Using the RSF for each element I applied the following formula to determine the elemental abundance in the sample:

$$\left(\frac{E}{E_0}\right)_{sample} = \frac{\left(\frac{I'_E}{I'_{E_0}}\right)_{sample}}{RSF\,(E, E_0)} \qquad \text{with } I'_E = I'_E{}^{ON} - I'_E{}^{OFF}$$

All this work allows me to have access to the elemental composition relative to Fe for every particle. In order to check the processes undergone by a given sample, it is usual to compare its elemental abundances to the elemental composition of CI chondrites, the most primitive carbonaceous chondrites (or more precisely the least thermally altered meteorites). This allows me to obtain, at the end, the elemental abundances relative to Fe and CI. The values for the elemental composition relative to Fe in the CI-type chondrites that I used are the ones provided by Lodders et al., 2010.

3.1.5 Error bar estimation

There are several origins for the uncertainty in the final value of the elemental abundance relative to Fe and CI for each element. First of all, there is an error bar on the measure of the relative sensitivity factor of the standard, -which is given in Bardyn et al., 2017. Then, there is also an uncertainty on the elemental abundances relative to Fe in the CI-type chondrites (Lodders et al., 2010). Finally, when the pipeline fits spectra, the algorithm gives a systematic error which corresponds to a statistical error linked to the number of counts on the given fitted peak, and a systematic error linked to the quality of the fit.

Hence, I considered the largest source of uncertainty.

3.1.6 Mapping methodology

After all this calculation, I studied (only for the Allende particle) each spectrum separately. Using the same fitting procedure as for the sets of spectra ON and OFF and, after the same normalization on the highest peak intensity (m/z = 73.05) of PDMS from the set of spectra OFF, I was able to plot the peak intensity of O, Na, Mg, Al, Si, Ca, Fe and Ni as a function of the position on the sample.

3.2 Raman data processing

During all this work, all Raman data have been processed with the help of the WiTec Project *Four* software.

First of all, before each measurement, I measured a Raman spectrum on a calcite reference mineral. This measurement allowed me to check the instrument calibration and to know the difference between the theoretical and experimental positions for each peak of the reference (see table 3.1 and figure 3.4). Therefore, every sample Raman spectrum has been corrected by the mathematical formula deduced from the reference mineral measurement.

Theoretical position (cm^{-1})	experimental position (cm^{-1})
156	154.8
282	282.4
713	714.4
1087	1089.1

Table 3.1: example of a difference between the theoretical and experimental peak positions for the reference mineral

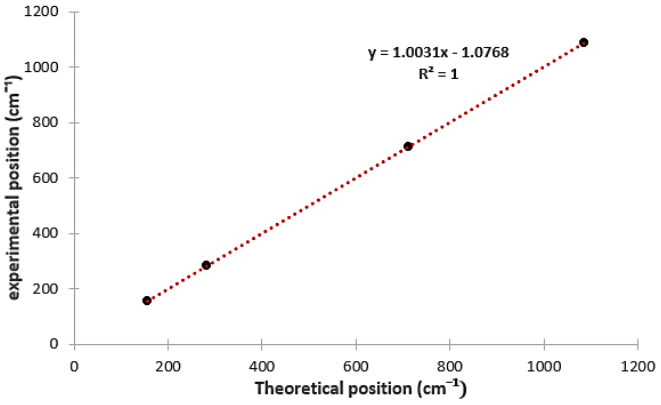

Figure 3.4: experimental position as a function of the theoretical ones.

Then, once my sample spectrum has been corrected, I processed it by removing the cosmic rays and by subtracting the background (see figure 3.5) by using two functions of the software (cosmic ray remover and graph background subtraction).

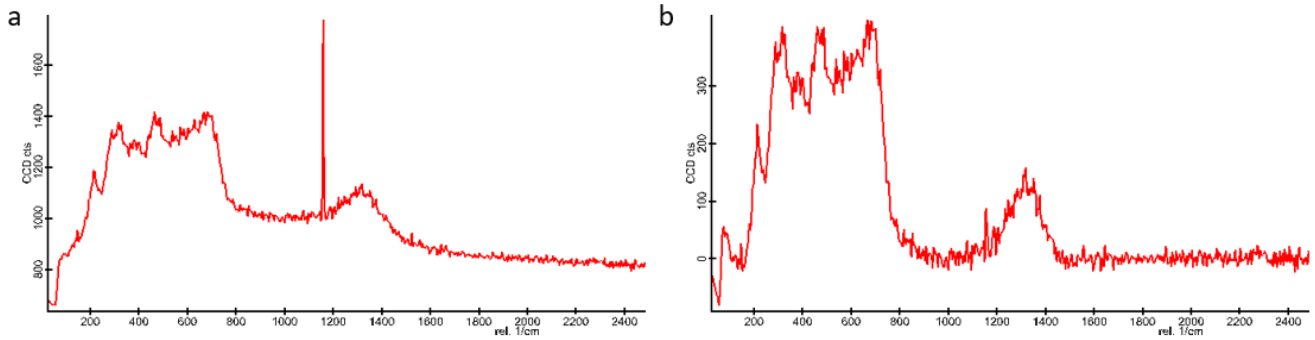

Figure 3.5: Raman spectra took at the same position for the same sample (a) before and (b) after the cosmic ray and the background correction.

Furthermore, after an image scan measurement, this software allows me to produce mappings of the compounds either by the selection of an entire peak (for example, the green region in figure 3.6) or by the selection of a precise position (for example, the blue region in figure 3.7). After the mapping, the software also allows me to combine one or several Raman maps with an optical image of the sample which gives me the spatial distribution of the compounds.

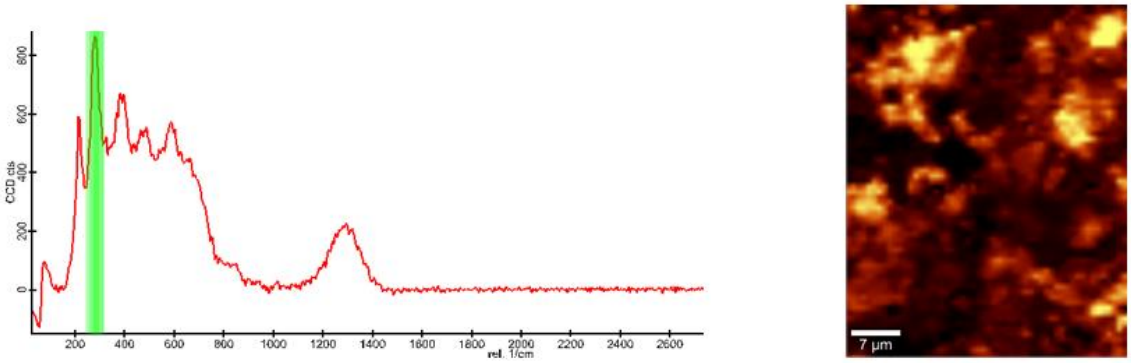

Figure 3.6: mapping (at the right side) of a selected peak on the Raman spectrum (at the left side)

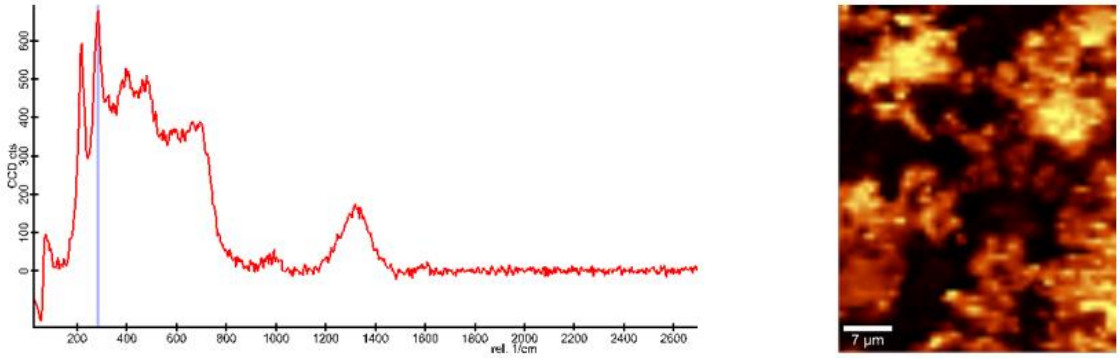

Figure 3.7: mapping (at the right side) of a selected position on the Raman spectrum (at the left side)

The last thing that I did with the Raman data is to identify the compounds present in the sample by comparing the measured spectra with Raman spectra of diverse minerals from the Rruff database.

For the three meteorites I measured with the Raman spectrometer, I also studied the organics signal. In a Raman measurement, organic material has mainly two different peaks: the G band and the D band. The spectral characteristics of these bands (position, full width at half maximum or FWHM, and relative intensity) depend on the material structure (graphitized and disordered) and, therefore, they give an indication on the thermal metamorphism of that sample has undergone. Thus, I needed to have access to the position of the two characteristic peaks (around 1350 cm^{-1} and 1600 cm^{-1}). I used the fitting routine of the software to fit those peaks by two Lorentz curves and gives me the parameters of the fit I am interested in: that is to say the position and the FWHM (see figure 3.8):

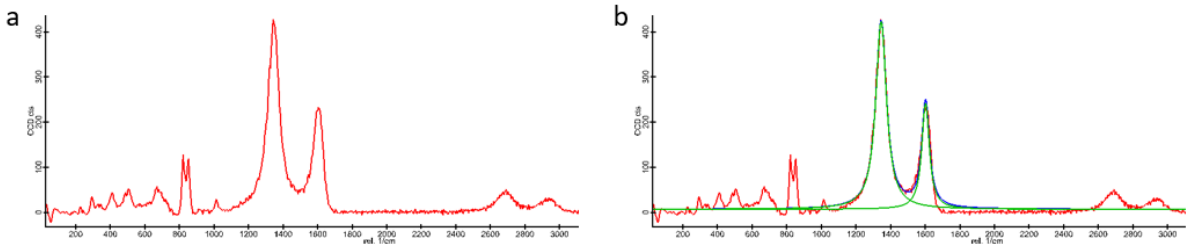

Figure 3.8: (a) Raman spectrum with the two organic peaks (around 1350 cm^{-1} and 1600 cm^{-1}) and (b) Raman spectrum with the two organic peaks fitted (green curves). The blue curve is the sum of the two Lorentzian curves.

3.3 Infrared spectra

The last technique that I used is the infrared spectroscopy. As mentioned previously, the measure of eleven infrared spectra taken on a Murchison sample, described in Stenzel et al., 2017, were freshly available and I thus processed and analyzed these data to compare them with the Raman data described in Stenzel et al., 2017

3.3.1 Spectra selection

During the measurement, thirty spectra have been taken.

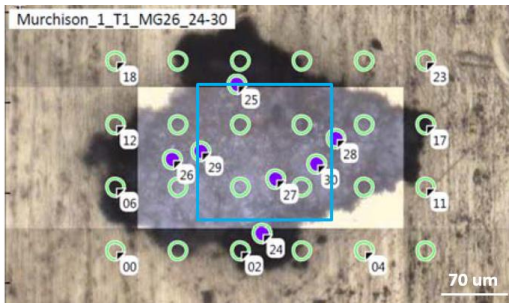

Figure 3.9: optical image of Murchison sample with the Raman mapping region (blue square) and the infrared spectra measurement positions (green circles)

In order to reduce the number of spectra, I chose those on the region where Raman measurements have been made (Stenzel et al., 2017). This zone is shown with the blue square on the figure 3.9. I also looked at a spectrum taken on the background.

So, at the end of the selection, I had to work with five spectra inside the Raman map, six spectra at the edge of this Raman map and one spectrum on the background.

3.3.2 Data analysis

Before any analysis of our spectra, it was necessary to look at the background spectrum (see figure 3.10) in order to know what peaks are present in the background and avoid any misunderstanding of the particle composition.

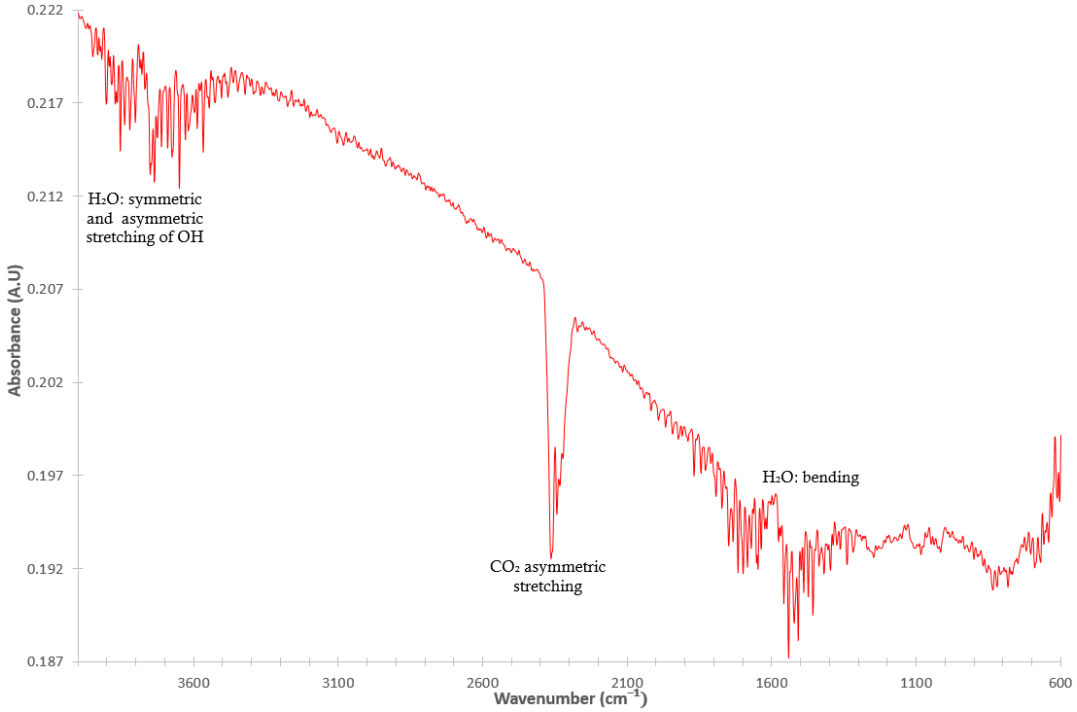

Figure 3.10: Infrared spectrum of the background with the assignment of the three main bands.

As we can see (figure 3.10), the signal to noise ratio is very low. Moreover, the baseline is not straight and so has to be corrected.

Then, the processing method was to compare the positions and relative intensities of all the detected peaks in each spectrum with spectra from different databases. This allowed me to assign to each peak a chemical bond and then predict the associated chemical function. This work is an attempt at identification of some of the minerals present and of the chemical functions that can be found in the organic matter but it does not give the exact nature of the organic material.

3.3.3 Mapping methodology

Finally, in order to do a direct comparison with the Raman study made on this sample, I mapped some of the identified chemical bonds using the following methodology:

i. Normalization of every spectrum to a common peak (that is to say σ = 1099.2 cm^{-1}).
ii. Selection of a set of spectra which show the chemical bond of interest.
iii. Correction of the baseline for the selected peak using the *Subtract Straight Line* command on the Origin software (see figure 3.11).
iv. Mapping the relative intensity of the corrected peak.

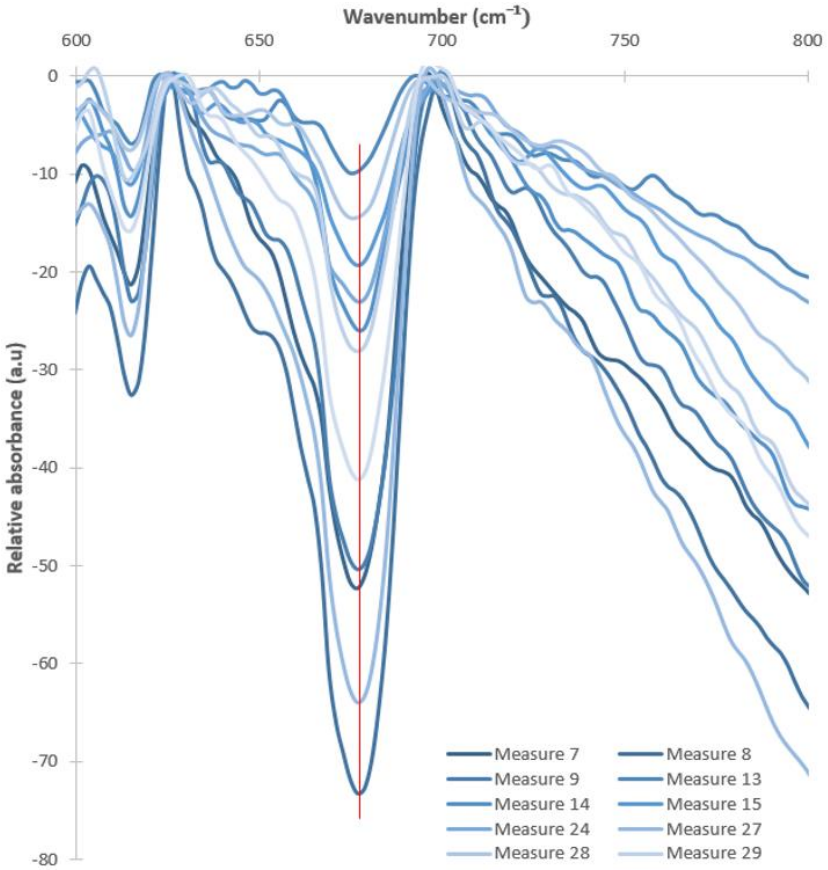

Figure 3.11: Infrared spectra with a baseline correction for the peak at σ = 677 cm^{-1}.

4 RESULTS

4.1 Antarctic micrometeorites sample characterization

The two Antarctic micrometeorites have been studied with a Raman spectrometer and an electron microscope with energy dispersive X-Ray spectrometer (SEM-EDX) by Günther et al., 2017.
Furthermore, these micrometeorites have been analyzed in ToF-SIMS using the ground model of COSIMA. By using the methods described in the previous section of this report, I have measured the elemental abundances relative to Fe and CI for different minerals and organics forming elements: C, O, Na, Mg, Al, Si, K, Ca, Ti, V, Cr, Mn, Fe, Co and Ni. The results can be seen in the figure 4.1.

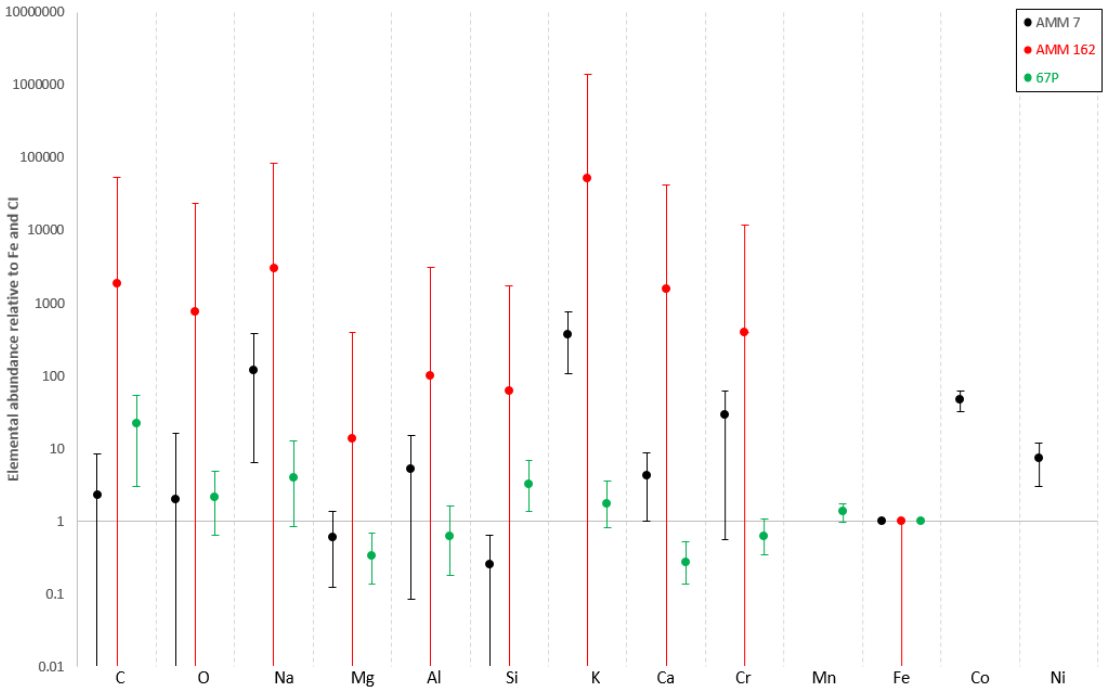

Figure 4.1: AMM 7 (black), AMM 162 (red) and comet 67P (green). The results represent the relative ratio $(X/Fe)_{AMM}/(X/Fe)_{CI}$ where $(X/Fe)_{AMM}$ corresponds to the elemental abundances relative to Fe in the sample and $(X/Fe)_{CI}$ corresponds to the elemental abundances relative to Fe in the CI-type chondrite (Lodders et al, 2010). For those three particles, we did not detect any signal for the Ti and V. the error bar on the AMM data is determined as explained previously but the largest source of uncertainty (especially for AMM162) is due to the low statistic.

For this plot of AMM7 and AMM162, it is necessary to be careful about the relative abundance of Na and K because, as explained in the previous part, these AMMs might have been contaminated by Na and K from the glass slides in which they have been stored.

4.2 Carbonaceous chondrites sample characterization

During the internship, I had to do several studies with different techniques on three different meteorites: Lancé, Allende and Murchison. These carbonaceous chondrites have been previously analyzed with SEM-EDX and it was necessary to perform Raman measurements on those same samples to characterize the minerals bearing the observed elements in the EDX mappings.

Furthermore, the ToF-SIMS spectra of five carbonaceous chondrites (Lancé, Allende, Murchison, Orgueil and Renazzo) have been measured before my arrival and my work has consisted in processing these data and measuring the elemental abundance in these meteorites.

Finally, during my internship, I did a study of eleven infrared spectra taken on a Murchison sample, described in Stenzel et al., 2017.

4.2.1 ToF-SIMS data

In order to compare the two micrometeorites with the five meteorites, I processed, for each five meteorites, the ToF-SIMS spectra with the exact same method than I did for the AMMs. Thus, I was able to measure the elemental abundances of the same elements relative to Fe and CI chondrites. It was also possible to compare the obtained abundances with the elemental abundances in the dust of comet 67P measured by COSIMA on-board the Rosetta spacecraft (Bardyn et al., 2017). This comparison is shown in the figure 4.2.

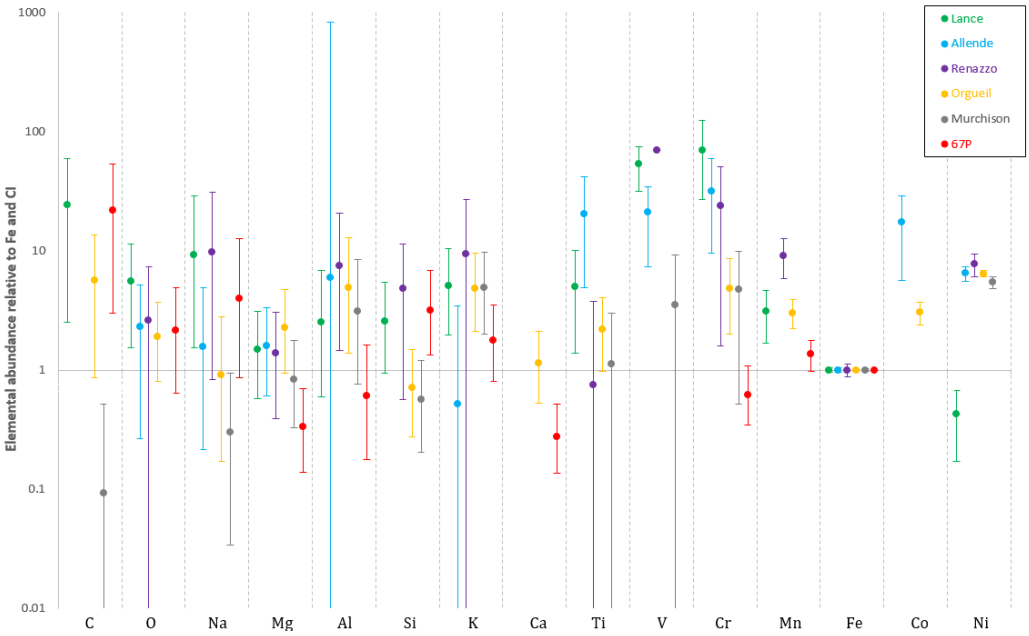

Figure 4.2: elemental abundance relative to Fe and CI chondrites for Lancé (green), Allende (blue), Renazzo (purple), Orgueil (yellow), Murchison (gray) samples and for 67P comet (red) from Bardyn et al., 2017. The errors bars for 67P data is due to the RSF's uncertainties (Bardyn et al., 2017) and, for meteorites, the largest source of uncertainty (like for AMMs) is due to the statistic

Furthermore, for the Allende sample, I also mapped the relative intensities of the elements detected. Those maps can directly be compared to the ones obtained with the electron microscopy technique (Günther et al., 2017). The figure 4.3 shows an example of such comparison between the SEM-EDX map and the ToF-SIMS map for iron. I mapped seven other elements that are shown in the appendix (figure A).

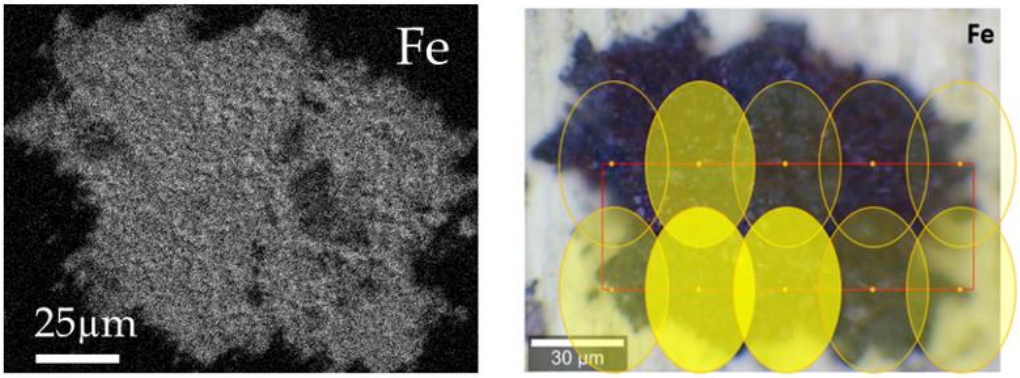

Figure 4.3: Left side: SEM-EDX mapping of Fe. Right side: ToF-SIMS mapping of Fe. The shape and the size of the yellow ellipse is the representation of the ion beam (35µm×50µm).

4.2.2 Raman measurements

The first work with the Raman technique was to identify the global mineral composition of three meteorites (table 4.1).

	Lancé (figure 4.4)	**Allende** (figure 4.5)	**Murchison**(figure 4.6)
Identified compounds			
	• Iron oxide: hematite • Pyroxene : augite • Olivine: forsterite • Organics	• Iron oxides: hematite (red) and magnetite (green) • Olivine • Pyroxene • Organics	• Iron oxide • Olivine • Pyroxene • Organics
Detailed chemistry			
Pyroxene	Augite: $En_{43,7}Fs_{37,5}Wo_{18,8}$ to $En_{44,1}Fs_{37,3}Wo_{18,6}$	Augite: $En_{43,7}Fs_{37,5}Wo_{18,8}$ to $En_{43,7}Fs_{37,3}Wo_{18,6}$	Enstatite: $En_{83}Fs_{17}$ to $En_{85}Fs_{15}$
Olivine	Forsterite: $Fo_{90\pm0,3}$	Forsterite: $Fo_{90\pm0,3}$	Forsterite: $Fo_{90\pm0,3}$

Table 4.1: global mineral composition of three different samples: Lance, Allende and Murchison.

It should be noted that the notations $En_xFs_yWo_z$ represent the chemical composition of the pyroxenes in terms of x, y and z% of the three poles. Enstatite (En, Mg pure pole, Ferrosilite (Fs, Fe pure pole) and Wollastonite (Wo, Ca pure pole). The notation Fo_x represents the chemical composition of the olivine in terms of the x% of the Mg pure pole Forsterite (Fo).

The comparison between the measured spectra and the RRUFF spectra are presented in the following figures (figure 4.4, 4.5 and 4.6). The spatial distribution of each minerals identified in the samples can be found in the appendix part (figure B, C and D).

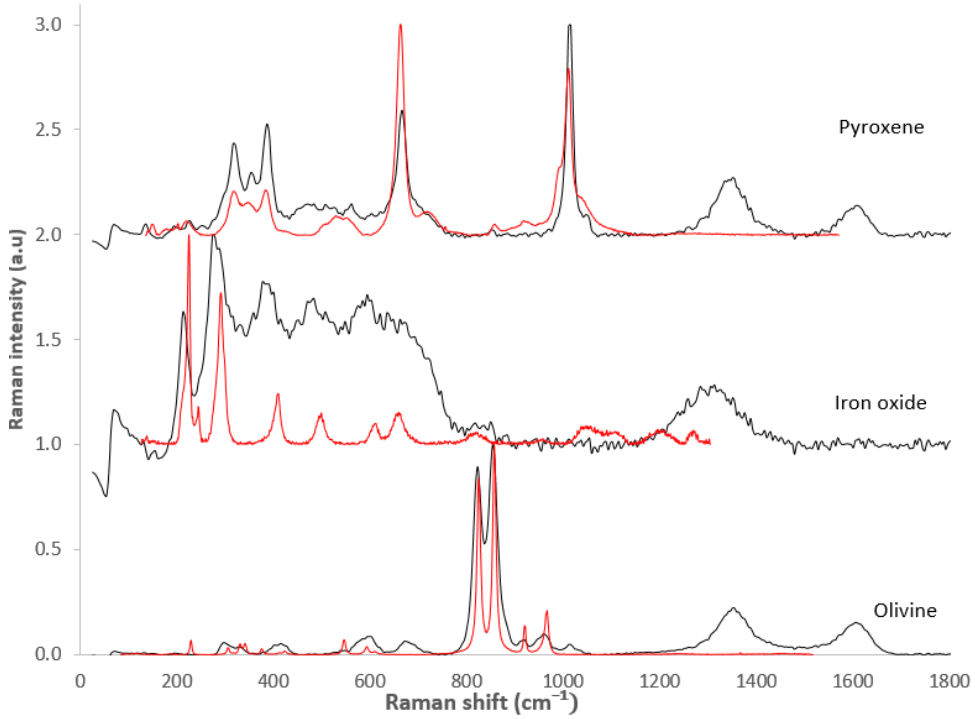

Figure 4.4: Raman spectra of identified minerals found in the Lancé sample (in black) compared with Raman spectra from the RRUFF database (in red).

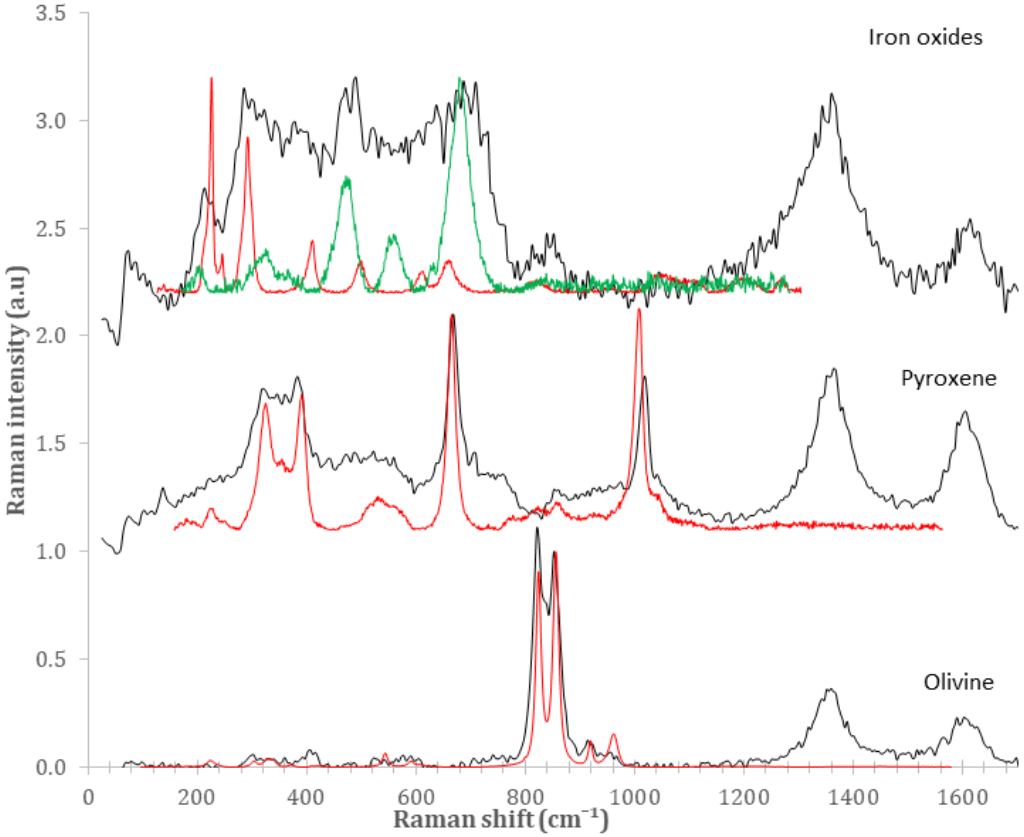

Figure 4.5: Raman spectra of identified minerals found in the Allende sample (in black) compared with Raman spectra from the RRUFF database (in red and green).

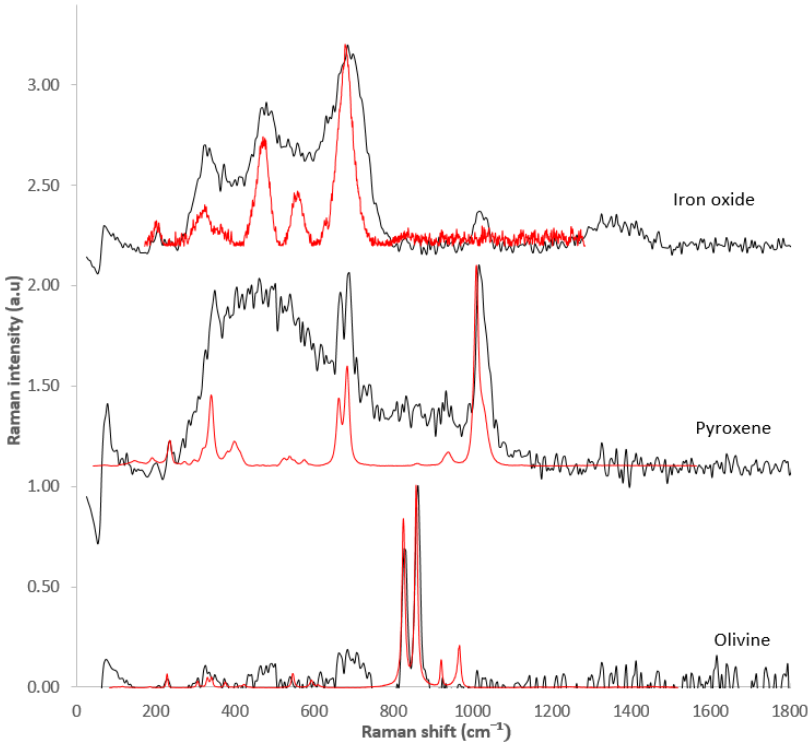

Figure 4.6: Raman spectra of identified minerals found in the Murchison sample (in black) compared with Raman spectra from the RRUFF database (in red).

For the Murchison sample, I also performed a 3D mapping which allow mapping the whole surface of the sample even if it has a complicated topography, thus, avoiding that some parts remain out of focus when performing simple 2D mappings. In order to map the spatial distribution of each compound, I used a characteristic peak of the compounds. For the olivine, I used the peak at 826 cm^{-1}, for the pyroxene, I used the peak at 1008 cm^{-1} and for the iron oxide, I used the peak at 682 cm^{-1}. The 3D mappings seen with different orientations are shown in figure 4.7.

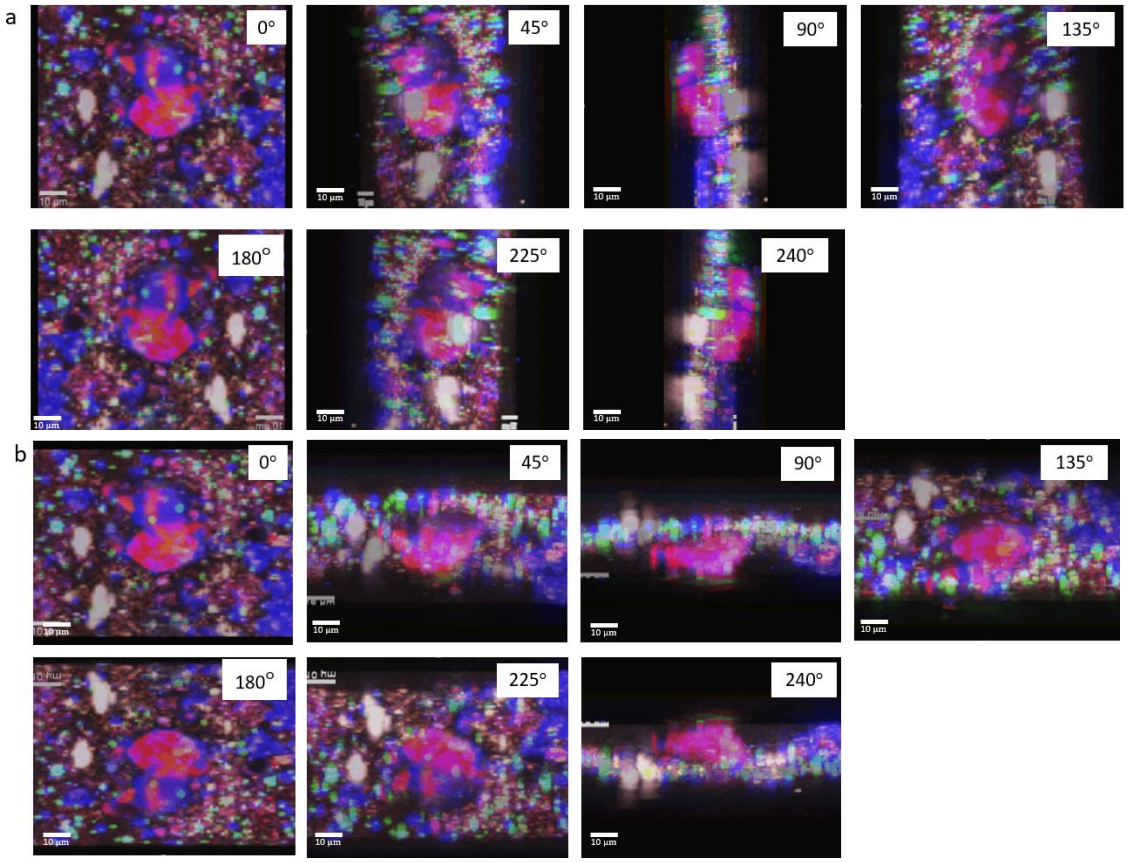

Figure 4.7: 3D projection along the Y (a) and the X (b) axis of the Raman mapping for olivine (red), iron oxide (blue), organics (green) and pyroxene (light pink).

Once the global mineralogical compositions of the Allende and the Lancé samples were known, I was able to look at small, unidentified inclusions, with a higher spatial resolution using a bigger objective (×100 compared to ×50 for the global mapping) in order to separate the signal from these inclusions from the surrounding minerals.

First of all, I worked with the Lancé meteorite. In the map of this particle with the ×50 objective, I was able to observe the presence of an inclusion but, because of the spatial resolution (1µm), I was not able to separate this compound from its neighbors (see figure E in the appendix). It was therefore difficult to identify correctly the inclusion. However, I was able to isolate it by performing a mapping with the ×100 objective. Hence, I was able to identify the inclusion as a feldspar mineral and more precisely as an anorthite: $(Ca_{0.94}Na_{0.04}Fe_{0.02})(Al_{0.98}Si_{0.02})\ Si_2O_8$ (see figure 4.8). Furthermore, it is possible to observe other peaks on the experimental spectrum which correspond to magnetite (peak around 666 cm^{-1}) and forsterite (peaks around 820 and 850 cm^{-1}).

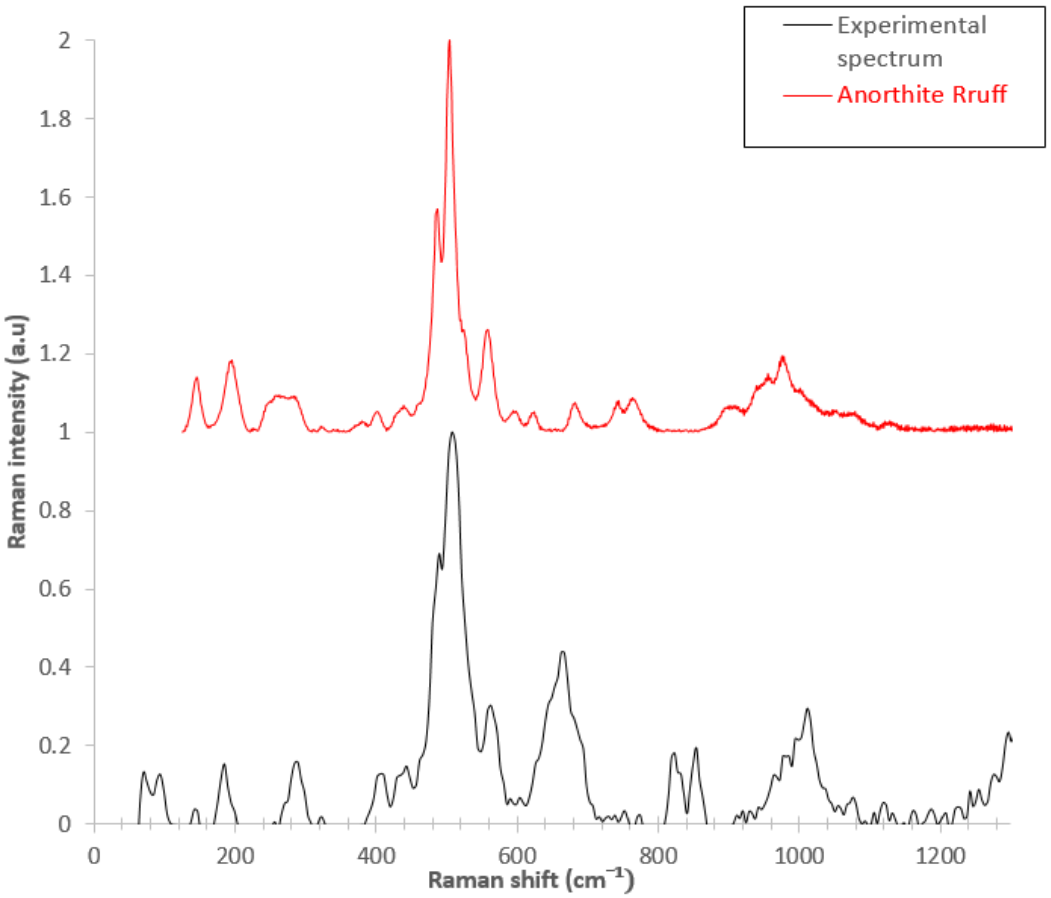

Figure 4.8: Raman spectrum of the anorthite inclusion found in Lancé sample.

I have then continued the identification work with the Allende meteorite. Previous measurements carried with the electron microscope with energy dispersive X-Ray spectrometer showed the presence of a region enriched in Na and Al and a second region enriched in Ni and S (SEM-EDX mapping are available in the appendix: figure F). The compounds that could bear these elements were not identified in the Raman global mappings of Allende which were carried out with the ×50 objetive. I thus performed measurements on these two regions with a ×100 objective in order to identify in the Raman data the minerals that could bear these elements. The detected compounds are shown in figure 4.9.

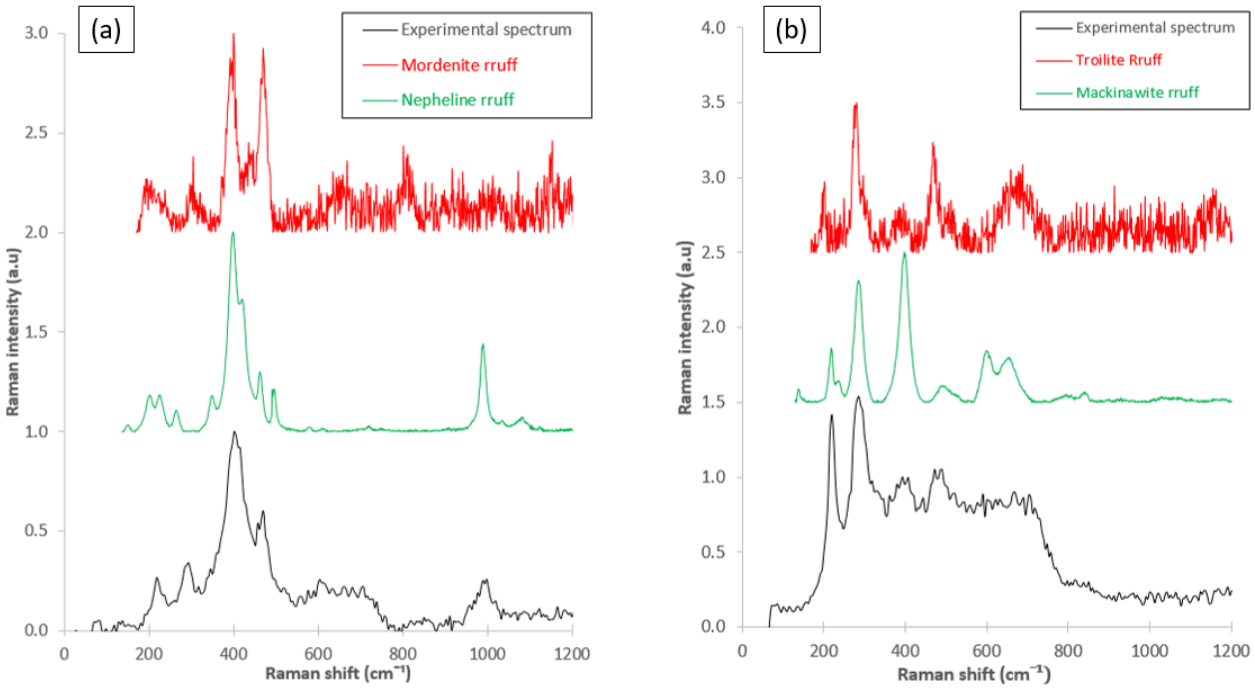

Figure 4.9: Raman spectra of the experimental compounds (black) and spectra from the Rruff database (red and green). The right side plot corresponds to the identification of the compound in the Na, Al rich region and the left side plot corresponds to the Ni, S rich region.

As we can see, the Na and Al rich region can be explained by the presence of a silicate. It can either be a nepheline, which is a tectosilicate and its formula is $(Na_{0.77}K_{0.23})_{\Sigma=1}Al_1Si_1O_4$ or either be a mordenite which is a zeolite and its formula is $(Na_{5.47}Ca_{0.29}K_{2.01})_{\Sigma=7.77}(Al_{8.06}Si_{39.94})O_{96}\cdot 28H_2O$. Since the uncertainty of the peak position at 402 cm^{-1} is 3 cm^{-1}, it is not possible to decide between these two compounds as the main peak of nepheline and of mordenite are located at 399.3 cm^{-1} and 399.4 cm^{-1} respectively.

Concerning the Ni, S rich region (figure 4.9 (b)), two different identifications are possible. In both cases, the Ni, S rich region can be explained by the presence of a sulfide mineral. However, it could either be a troilite and its formula is FeS or either be a mackinawite and its formula is $(Fe, Ni)_{1+x}S_{x=0-0.07}$. We can compare the uncertainty on two different peaks. For the first one, the experimental spectrum has a peak at 285.2 cm^{-1} while the Troilite shows this same peak at 279.4 cm^{-1} and the mackinawite at 285 cm^{-1}. For the second one, the experimental spectrum has its peak at 392.8 cm^{-1} while the troilite shows this peak at 279.4 cm^{-1} and the mackinawite at 397.8 cm^{-1}. It is again not possible to decipher which of these sulfides is present in the sample.

Finally, the last work that I was able to do with the Raman measurement was about the organics peaks. For each of the three meteorites, I measured the position and the full width half maximum of the G and D bands. I was able to compare the measured values with literature values for these three meteorites (Busemann et al., 2007) in order to know if the organic material present in these samples is representative of the bulk meteorite. I could also compare the three meteorites with the Antarctic micrometeorites AMM7 and AMM162 (Günther et al., 2017). Figure 4.10 shows the FWHM of the G band against its position in the measured samples. The literature values are also reported on this plot.

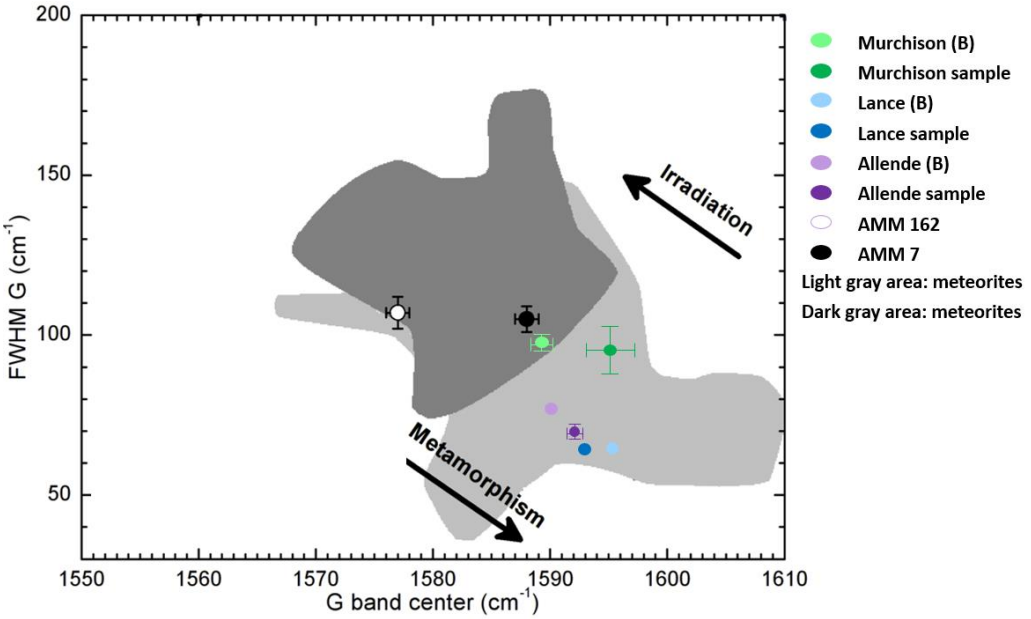

Figure 4.10: FWHM of the G band vs. its position for Lancé, Allende and Murchison compared to the value for the bulk meteorite (Busemann et al., 2007) and for the two Antarctic micrometeorite (Günther et al., 2017). This plot is adapted from Rotundi et al., 2008. The light and dark gray areas are respectively the regions that correspond to the carbonaceous chondrites and to interplanetary dust particles. Ordering aromatic matter by thermal metamorphism tends to shift the G band toward higher wavenumbers and make it narrower. Disordering matter (after irradiation by high-energy particles for example) has the opposite effect.

For Murchison, it is necessary to be careful because parts of the sample were lost during the sample preparation and only traces are left. The organic signal was found in these traces and not directly on the meteorites fragments. Thus, we cannot be sure that this signal corresponds to the meteoritic organic and not to the terrestrial contamination. This might explain the difference between the measured and the literature value.

4.2.3 Infrared data

Finally, the last study was the processing of infrared spectra for a Murchison sample. In the following, I will illustrate the data processing with one of the IR spectra but the method applies to all spectra. As described in the method section, I tried to assign every band to a chemical bond by comparing the positions and relative intensities with spectra from available databases. The figure 4.11 shows that work for the spectrum number 13 and the rest of the study is given in the form of a recapitulative chart in the appendix part (table A).

Moreover, for each spectrum, I decided to separate the study according to the two different spectral features we observed (see material and theory section): the first one is from 4000 cm^{-1} to 1200 cm^{-1} (the Reststrahlen bands) and the second one is from 1200 cm^{-1} to 600 cm^{-1} (the Absorption bands).

Figure 4.11: Reststrahlen bands (a) and absorption bands (b) of the spectrum number 13 with the roman number corresponding to each peak assigned in the **table 4.2 and 4.3**.

Band	Band position (cm-1)	Assignement	Chemical group or mineral	Band	Band position (cm-1)	Assignement	Chemical group or mineral
I	3670 – 3650	O—H stretching	Phyllosilicate	XIII	2370 – 2330	C—O stretching	Co_{atm}
II	3630 – 3600			XIV	2160 – 2100	-C≡C- stretching	Alkyne
III	3560 – 3520	Fe^{3+}— Fe^{3+}—OH Fe^{3+}— Fe^{2+}—OH	Celadonite	XV	2060 – 1970	C=C=C stretching	Allene
IV	3620 – 3060	O—H stretching	Absorbed water	XVI	1980 – 1900	C—O stretching	
V	3260 – 3230	C—H stretching	Alkyne	XVII	1830 – 1800	??	Carbonate
VI	3180 – 3150	??	??	XVIII	1790 – 1750	??	??
VII	2990 – 2960	CH_3 asymmetric stretching	Aliphatic	XIX	1750 – 1700	C=O stretching	Ester or ketone
VIII	2950 - 2910	CH_2 asymmetric stretching	Aliphatic	XX	1670 – 1580	C=C stretching	Alkene
IX	2870 - 2830	CH_3 symmetric stretching	Aliphatic	XXI	1450 – 1390	CO_3 stretching	Carbonate
X	2760 – 2620	O—H stretching	Carboxylic acids	XXII	1380 – 1350	CO_2^-	Carboxylic acid
XI	2460 – 2380	??	??	XXIII	1320 - 1280	C=O stretching	Ketone
XII	2320 – 2250	CO_2 asymmetric stretching	Air contamination	XXIV	1240 – 1200	C—O stretching	Carboxylic acid

Table 4.2: Assignment of the bands for the Reststrahlen bands of the spectrum number 13

Bands	Band position (cm-1)	Intensity	Profile	Assignement	Mineral
I	1115 – 1090	Strong	Sharp	Si—O stretching	Celadonite
II	1080 – 1060	Strong	Shoulder	Si—O stretching	Celadonite
III	960 – 920	Strong	Broad	Si—O stretching	Celadonite
IV	890 – 870	Weak	Sharp	??	Carbonate or olivine
V	810 – 790	Medium	Sharp	Fe3+—Mg—OH bending Fe3+— Fe2+—OH bending	Celadonite
VI	750 – 730	Medium	Broad	Al—O—Si bending	Celadonite
VII	720 – 710	Medium	Sharp	??	Carbonate
VIII	680 – 670	Medium	Sharp	Si—O stretching	Pyroxene
IX	650 – 630	Medium	Sharp	Si—O stretching	Pyroxene
X	620 – 600	Medium	Sharp	Si—O stretching	Pyroxene

Table 4.3: Assignment of the bands for the absorption bands of the spectrum number 13

Finally, I could produce mappings of some compounds or chemical bounds in order to see the localization of the minerals and of the organic material in the sample (figure 4.12). More mappings can be found in the appendix (figure G).

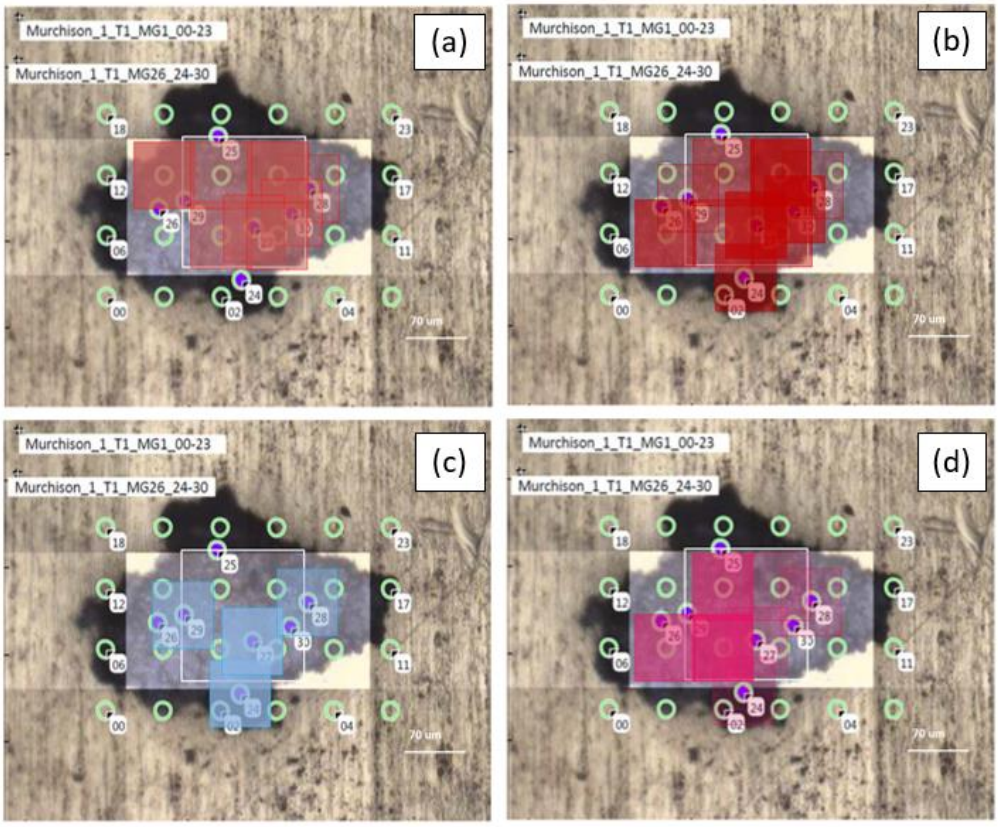

Figure 4.12: Infrared mapping of (a) phyllosilicate mineral, (b) CH_2 stretching for a carbonyl group, (c) pyroxene mineral and (d) C-O-C stretching. The size of the colored squares is the representation of the spot size (70µm×70µm). Furthermore, their intensity is proportional to the intensity of the peak in the spectra.

5 DISCUSSION

In this section, I will use the results presented in the previous section to compare the two AMMs with cometary data from COSIMA and with the five carbonaceous chondrites in order to speculate on the potential origin of the micrometeorites that I have studied.

5.1 AMMs compared to comet 67P with ToF-SIMS measurements

The elemental abundances measured in the two AMMs (figure 4.1) are very different and might reflect different parent bodies and/ or different terrestrial processing.

I will first focus on the AMM7. Figure 4.1 shows the comparison of the elemental abundances measured in AMM7 with the elemental abundances in CI carbonaceous chondrites. The elemental abundances in AMM7 are close to the chondritic values as they are within a factor of 10 of the CI values. However, we can observe an enhancement of Na and K in AMM7 compared to the CI values which could be due to contamination from the glass slides in which the AMM has been stored.
Furthermore, as we can see in figure 4.1 and 4.2, AMM7 shares similarities with the cometary particles. However, the Mg to Si ratio seems chondritic for AMM7 (Mg/Si = 2.4) which is not the case for the comet (Mg/Si = 0.1).
Moreover, AMM7 is less rich in carbon than the cometary particles (C/ Fe = 2.3 for the AMM7 compared to C/ Fe = 21.8 for 67P) and is more consistent with the CI value.

Thus, based on elemental abundances, AMM7 seems to share properties with CI chondrites and could originate from the same parent body than these meteorites rather than from a comet.

Then, we can focus on the second micrometeorite, the AMM162. As we can see in figure 4.1, this sample is enriched in all elements compared to the CI chondrites by more than a factor of 10 and, therefore, it is not chondritic. We can also conclude that AMM162 is unlikely to originate from a comet either as the elemental abundances measured in AMM162 are very different from the ones measured in the cometary particles. However, we can see that the Na and K abundances are particularly high. This result could be due to a similar contamination than for AMM7 from the storage. However, it could also be due the presence of (Na, K) sulfates as they have been detected in Raman (Günther et al., 2017). The origin of the sulfate minerals is unclear. We cannot, indeed, exclude some terrestrial weathering as sulfates are a common product of terrestrial weathering (Rubin et al., 1997). If sulfates are indigenous, it could be an indication of an aqueously altered parent body. Furthermore, this particle is smaller than the COSIMA beam size (23µm x 20µm x 29µm). Therefore, one has to be careful that the contribution of the contamination of the target was not underestimated.

From the elemental abundances, I can conclude that AMM162 is unlikely to have come from a comet or from the same type of parent body as the CI chondrites.

5.2 AMMs compared to carbonaceous chondrites

5.2.1 ToF-SIMS measurements

The comparison of the elemental abundances measured in the two AMMs and in the five chondrites are shown in figure 4.2. Thereby, it is possible to compare AMMs with the different types of carbonaceous chondrites.

As stated in the previous paragraph, AMM162 is not chondritic and, therefore, cannot be compared to any of the carbonaceous chondrites measured here.

However, we are now able to compare AMM7 with our five chondrites. As we can see in the figure 4.2, the elemental composition of AMM7 is closer to the ones measured for Orgueil and Murchison for most of the elements (C, O, Mg, Al, Si, Ca, Cr and Ni). There is only an exception for the abundance of Na and K which are higher for the AMM than for the meteorites, as explained in the previous paragraph. It is thus possible that this AMM shares similar origins than CI (Orgueil) and CM (Murchison) type of chondrites.

It is now interesting to see if the elemental composition resemblance that we observe between the AMM7 and Orgueil and Murchison is also true regarding the mineralogical and organic composition.

5.2.2 Raman measurements

Raman measurements of the AMM7 have been performed before I arrived to the institute (Günther et al., 2017). They were able to identify pyroxene and more precisely $En_{50}Fs_{50}$ (i.e. $(Mg_1Fe_1)_{\Sigma=2}Si_2O_6$) to $En_{90}Fs_{10}$ (i.e. $(Mg_{1.8}Fe_{0.2})_{\Sigma=2}Si_2O_6$), olivine ($Fo_{37\pm19}$ to $Fo_{99\pm16}$) but also iron oxide (hematite). Finally, Günther et al., 2017 conclude that AMM7 is close to a CI and CM type chondrites regarding the mineralogical composition.

I performed Raman measurements on the same fragment of Murchison than the one that has been used for the ToF-SIMS study. At the end of this work, I was able to observe also pyroxene identified as $(Mg_{0.84}Fe_{0.16})(Si_{0.99}Al_{0.01})O_3$ (in other word : $En_{84}Fs_{16}$), olivine identified as $(Mg_{1.82}Fe_{0.18})_{\Sigma=2}SiO_4$ (in other words Fo_{90}) and hematite (and magnetite) among iron oxides. Hence, the global mineral composition of the AMM7 is close to the one measured for Murchison.

Furthermore, the carbonaceous material was also studied (see figure 4.10). As we can see, the spectral characteristics of the G band for AMM7 are close to the ones in Murchison which indicate that they might have undergone a similar degree of thermal metamorphism.

Finally, the AMM162 Raman studies have also been performed and have showed the presence of Ca-rich pyroxene and (Na, K)-rich sulfates (Günther et al., 2017). These results, even if they are not comparable to our meteorite composition, are consistent with the ToF-SIMS measurements that showed an enhancement of Na, K and Ca. Furthermore, the spectral characteristics of the G bands (shown in figure 4.10) indicate a more disordered material than for AMM7 which could be the consequence of an irradiation by high-energy particles.

5.3 Spectroscopic data interpretation

When analyzing the composition of a sample with a given technique, some information remains inaccessible due to the lack of sensitivity of the given technique to some materials. It is thus important to know what are the limitations of the technique used in order to properly interpret the data. In this last section, I will compare the different techniques that have been used for this work.

5.3.1 Raman and electron microscopy with energy dispersive X-Ray spectroscopies

When I studied the Allende particle, I used the complementarity between Raman spectroscopy and SEM-EDX. Raman mappings are very long to perform and thus usually do not allow full mappings of a large sample with a very high spatial resolution. We can therefore only have access to the global composition. Thanks to the previous SEM-EDX measurements, which allow mappings of the distribution of elements at a very high spatial resolution, we observed some regions in the sample containing elements whose presence could not be explained by any of the materials identified in the Raman global composition mappings. These EDX mappings allowed me to identify the specific regions which should be mapped in Raman with a higher spatial resolution and thus the identification of the two inclusions.

Hence, even if the two methods do not give the same kind of information about the particle (compound identification possible with the Raman technique and the observation of the spatial distribution of elements with the SEM-EDX method), it is important to compare them in order to confirm an analysis with similar and/-or consistent results but also in order to perform a deep study of a sample.

5.3.2 Raman and Infrared spectroscopies

In this section, I will compare Raman and Infrared spectroscopy using the example of Murchison previously studied with the Raman method (Stenzel et al., 2017).

Once again, having two different measurements of the same sample allows the confirmation of an identification. As described in the method section, our infrared data have a low signal to noise ratio. Furthermore, each spectrum shows the presence of many chemical bounds. It is, therefore, interesting to have another method that can be used to confirm the identification made with the IR spectra. The previous Raman measurements have given the Raman mapping of the pyroxene (see figure H in the appendix section) and I have been able to map the same compound from the infrared data (see fig. 4.12 (c)). The spatial distribution of this mineral is consistent in both studies which confirms the infrared assignment.

Furthermore, the two techniques can be complementary. First of all, we can focus on the organic material. With the Raman method, it was possible to observe organic signal (the D and G bands) but also to map it in order to know the spatial distribution of this material. However, the D (disordered) band (around 1350 cm^{-1}) and the G (graphitized) band (around 1600 cm^{-1}) corresponds to the double bond C=C. Therefore,

even if we know that organics are present, we cannot characterize them more precisely. The infrared study allows me to identify many chemical bonds in the organic matter present in the sample and also allows analyzing its spatial distribution. Therefore, Raman and Infrared mappings can be compared (see figure 4.12 (b) and figure G and H in the appendix section). On one hand, I can confirm the origin of the infrared band (organic and not mineral) because organic Raman mappings and the compounds mapped from the infrared data have the same spatial distribution (unless the organic and the mineral components are associated to each other in some way). On the other hand, the comparison allows me to characterize more precisely, thanks to the infrared data, the Raman organic signal. For example, I was able to identify the presence of carboxylic acid, alcohol, amine or amide, hydrocarbon, ketone or aldehyde from the infrared data while these compounds were not observed in the Raman data.

Moreover, there is another example of the importance of the comparison between the two methods with the C-O-C bond mapping (figure 4.12 (d)). I was able to identify the C-O-C bond in the infrared spectra. However, I was not able to say if this signal corresponds to an organic or a mineral (like a carbonate for example). But, by comparing the infrared mapping for C-O-C bond with the Raman mapping for the organic part (figure H in the appendix section), I was able to observe that their spatial distribution was different which means that the C-O-C bond does not come from an organic compound, or that the organic compounds responsible for the C-O-C bond in the infrared spectra is a different compound than the one responsible for the D and G peaks in the Raman spectra.

Finally, the infrared study shows that it is necessary to be careful with the composition we conclude from the Raman measurements. In the Murchison case, I was able to observe a phyllosilicate signal with infrared spectra (see figure 4.12 (a)) that I did not observe in the Raman spectra. Therefore, the Raman method is not sensitive enough for all minerals and the absence of a signal does not necessarily mean that the component is absent.

5.3.3 SEM-EDX and ToF-SIMS spectroscopies

The last comparison that I can make is between SEM-EDX and ToF-SIMS measurements. Both techniques allow to access to the elemental abundances in a sample. However, COSIMA has a limited spatial resolution which makes it challenging to access to local composition variations within a sample. By comparing the ToF-SIMS measurements with EDX measurements taken in an electron microscope, we can get useful information for the interpretation of the COSIMA flight data. Bardyn et al., 2017 reported that the composition of 25 cometary particles shows some variations in Na, Mg and Fe but at the scale of COSIMA (about 40 µm), the particles are always a mixture of silicates and organic matter. It is thus interesting to check at what scale compositional heterogeneities are measurable with COSIMA, or in other words, can COSIMA detect variations in composition at a scale smaller than its beam size. Figure 4.3 and figure A in the appendix show the ToF-SIMS mapping of several element for the Allende sample which can be directly compared with the SEM-EDX mapping for the same elements taken on the Allende particle. As we can see, and even if it is not as clear on the ToF-SIMS mapping as it is on the SEM-EDX mapping, it is possible to have the spatial distribution of elements by using ToF-SIMS data.

Thanks to the high resolution of the SEM-EDX method, heterogeneities are measurable at several scales. First of all, I will focus on the Ca mappings. With the SEM-EDX method (figure A (b) in the appendix section), it is possible to observe a heterogeneity (13 µm x 10 µm) and it seems that it is also possible to observe it in the ToF-SIMS map (figure A (a) in the appendix section). Then, I will focus on the Fe mappings where the SEM-EDX shows a smaller heterogeneity (10 µm x 5 µm). Even if this one is smaller, it is still possible to observe it in the ToF-SIMS map. Finally, I will focus on the Na mappings. The heterogeneity that the SEM-EDX shows is smaller (5 µm x 4 µm) and, this time, it is not possible to observe it in the ToF-SIMS map.

Hence, since we know that the beam size is 35 µm x 50 µm, COSIMA is able to detect variations in composition at a scale smaller than its beam size. However, there is, either way, a limit of detection for the variation in composition within a sample.

6 CONCLUSION

During this internship, the principal objective was to analyze two Antarctic micrometeorites and to classify them among extraterrestrial material families by comparing them with cometary data and five different carbonaceous chondrites. In order to do so, I used four spectroscopic techniques from which I was able to deduce the elemental abundances and characterize both the mineral and the organic material. Along the study on the samples, I was able to also compare the different techniques together.

Thereby, I performed complementary Raman measurements on the Lancé and the Allende meteorites in order to characterize the precise nature of some inclusions present in the samples that have not yet been characterized. With the Raman technique, I was also able to perform the characterization of the Murchison sample.

Then, I processed the ToF-SIMS data of all the samples in order to measure the elemental abundances. Thanks to that processing, I was also able to map the elemental distribution in the Allende particle and so to compare them with elemental distribution obtained previously (Günther et al., 2017) using the SEM-EDX technique.

Finally, I processed Infrared data of a Murchison sample in order to identify mineral and organic compounds and compare these results with the ones obtained with Raman measurements on the same sample. At the end, I was able to map the spatial distribution of chemical bonds and compare it with the Raman mappings.

At the end of this work, I concluded that the AMM162 is very unlikely to originate from a comet or from the same parent bodies than carbonaceous chondrites. Similarly, AMM7 is unlikely to come from a comet, but I was able to show that this AMM seems to share properties with two carbonaceous chondrites (Orgueil and Murchison) which could indicate that the parent body of AMM7 is of the same type than for these two meteorites.

Moreover, the comparison between techniques showed that the possibility of having several pieces of spectroscopic information gives the opportunity to confirm the identification obtained from each technique (thanks to consistent results), to perform deeper study and to get more precise results. Furthermore, it also gave me information about the limitation of the techniques.

For the future, it will be interesting to continue the work by the process of negative ToF-SIMS spectra in order to quantify other elements like N or S. Furthermore, I showed that the ToF-SIMS elemental mappings give conclusive results with the Allende sample. Indeed, it has been possible to detect variations in the composition. It will be interesting to perform the same work on all the carbonaceous chondrites, on the AMMs but also on the cometary grains.

In addition, it would be interesting to get infrared data for all the other samples and continue the work of assignment in order to further characterize their mineralogy and organic content.

Finally, this internship was, personally speaking, an incredible and very enriching experience. Thanks to my supervisor (daily), and my entire team, help and support, I was able to grow as a scientist. I was able to work with four different spectroscopic techniques and to do physics, chemistry and to discover geology. Furthermore, this internship allows me to confirm my desire to work on an astrochemistry subject and to look for a PhD in astronomy.

REFERENCES

Bardyn A. (2016) *Caractérisation de la matière organique contenue dans les particules de la comète 67P/ Churyumov--Gerasimenko par spectrométrie de masse avec l'instrument COSIMA de la sonde Rosetta*, **Thèse de doctorat**.

Bardyn A., Baklouti D. et al (2017) *Carbon-rich dust in comet 67P/ Churyumov-Gerasimenko measured by COSIMA / Rosetta*, **Monthly Notices of the Royal Astronomical Society**, 469, p. S712-S722.

Brandstätter F., Ferrière L., Köberl C. (2012) *Meteorites : witnesses of the origin of the Solar System*, **Edition Lammerhuber**, 978-3-902421-68-5.

Brownlee D. et al. (2006) *Comet 81P/ Wild 2 under a microscope*, **Science**, 314, 1711.

Busemann H. et al (2007) *Characterization of insoluble organic matter in primitive meteorites by microRaman spectroscopy*, **Meteoritics and Planetary Science**, 42, -1387.

Caselli P., Ceccarelli C. et al (2012) *Our astrochemical heritage,* **Astronomy and Astrophysics Review**, 20, 56.

Cottin H. et al (2015) *Astrobiology and the Possibility of Life on Earth and Elsewhere*, ***Space Science Reviews,*** 1-42.

Duke D. A. et al (1964) *Infrared inverstigation of the olivine group minerals*, **The American mineralogist**, 49, 1388.

Fray N. et al (2016) *High-molecular-weight organic matter in the particles of comet 67P/ Churyumov-Gerasimenko*, **Nature**, 538, 72.

Günther S. et al (2017) *Composition of micrometeorites compared to carbonaceous chondrites and comet 67P/ Churyumov-Gerasimenko*, **European Planetary Science Congress**, 248.

Hilchenbach M. et al. (2016) *Comet 67P/Churyumov–Gerasimenko: Close-up on Dust Particle Fragments*, **The Astrophysical Journal Letters**, 816, L32.

Jung C. et al (1996) *The CO stretching mode infrared spectrum of substrate-free cytochrome P-450$_{com}$-CO. The effect of solvent conditions, temperature and pressure*, **Eur. J. Biochem**, 235, 660.

Kissel J. et al (2007) *COSIMA-High resolution time-of-flight secondary ion mass spectrometer for the analysis of cometary dust particles onboard Rosetta*, **Space Science Reviews**, 128, 823.

Krüger H. et al (2015) *COSIMA-Rosetta calibration for in-situ characterization of 67P/ Churyumov-Gerasimenko cometary inorganic compounds*, **Planetary and Space Science**, 117, 35.

Lafosse A. lesson, chapter II : Spectroscopie de vibration-rotation (IR) et spectroscopie rotationnelle (microondes)

Lodders K. et al (2010) *Solar system abundances of the elements.* . In: Goswami A., Reddy B. E. (eds) *Principles and perspectives in cosmochemistry*, **Spinger- Verlag**, p.379-417.

Ringwood A. E (1979) *Origin of the Earth and Moon*, **Spinger- Verlag**, p.295.

Merouane S. et al (2014) *Relations between aliphatics and silicate components in 12 stratospheric particles deduced from vibrational spectroscopy*, **The astrophysical journal**, 780, 174.

Oro J. et al (1961) *Comets and formation of biochemical compounds on primitive* Earth, **Nature**, 190, 389-390.

Rotundi A. et al (2008) *Combined micro-Raman, micro-Infrared, and field emission scanning electron microscope analyses of comet 81P/ Wild 2 particles collected by Stardust*, **Meteoritics and Planetary Science**, 43, 367.

Rubin A. E. et al (1997) *Mineralogy of meteorite groups*, **Meteoritics and planetary science**, 32, 231.

Salisbury J. W. et al (1989) *Mid-Infrared (2,5 to 25 μm) spectra of minerals*, **U.S Geological survey**, 87, 263.

Salisbury J.W. et al (1993) *Mid Infrared Spectroscopy: Laboratory Data*. In: Pieters C.M., Englert P.A.J. (eds.) *Remote Geochemical Analysis: Elemental and mineralogical composition*. **Cambridge University. Press**.

Sephton, M. A. (2002) *Organic compounds in carbonaceous meteorites*, **Natural Product Reports**, 19, 292.

Socrates G. et al (2004) *Infrared and Raman characteristics group frequencies: tables and charts*, **Willey**.

Stenzel O. et al (2017) *Similarities in element content between Comet 67P/ Churyumov-Gerasimenko Coma dust and selected meteorites samples*, **Monthly Notices of the Royal Astronomical Society**, 469, p.S492-S505

Tarantino S. C. et al (2002) *Mixing properties of the enstatite-ferrosilite solid solution: II. A microscopic perspective*, **Eur. J. Mineral**, 14, 537-547.

Weiszburg T. G. et al (2004) *Celadonite, the 10-Å green clay mineral of the manganese carbonate ore*, **Acta mineralogica petrographica**, 45, 65-80.

Willacy K. et al (2015) *The composition of the protosolar disk and the formation conditions for comets*, **Space Science Reviews**, 197, 151.

Maurette M. et al. (1991) *A collection of diverse micrometeorites recovered from 100 tonnes of Antarctic blue ice*, **Nature**, 351, 44.

https://chem.libretexts.org/Reference/Reference_Tables/Spectroscopic_Parameters/Infrared_Spectroscopy_Absorption_Table

http://jean-jacques.auclair.pagesperso-orange.fr/ftirUV/background.htm#

https://orgchemboulder.com/Spectroscopy/irtutor/alkanesir.shtml

https://orgchemboulder.com/Spectroscopy/irtutor/alkynesir.shtml

https://www.lachimie.fr/analytique/infrarouge/table-infra-rouge.php

APPENDIX

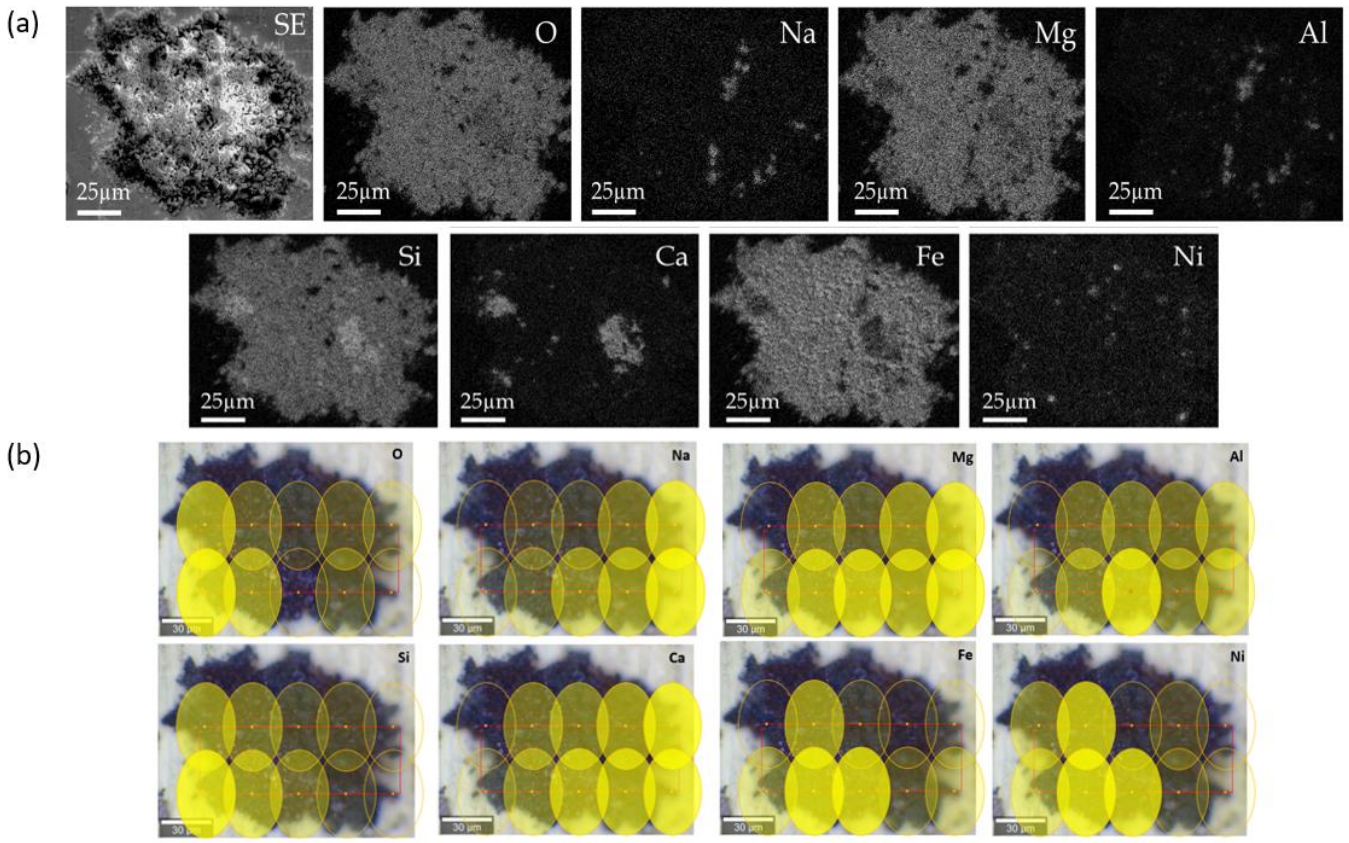

Figure A: (a) ToF-SIMS mapping. Top row (from left to right): ToF-SIMS mapping O, Na, Mg and Al. Bottom row (from left to right): ToF-SIMS mapping Si, Ca, Fe and Ni. (b) SEM-EDX mapping of the same elements. The shape and the size of the yellow ellipse is the representation of the ion beam (35µm×50µm).

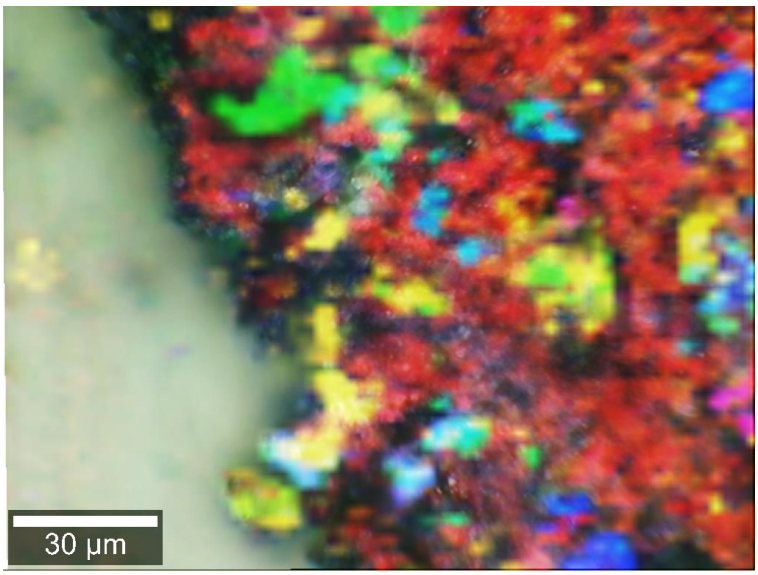

Figure B: Raman mapping for olivine (blue), iron oxide (red), pyroxene (yellow) and organics (green) on the Lancé sample. The x50 objective was used to perform this measurement.

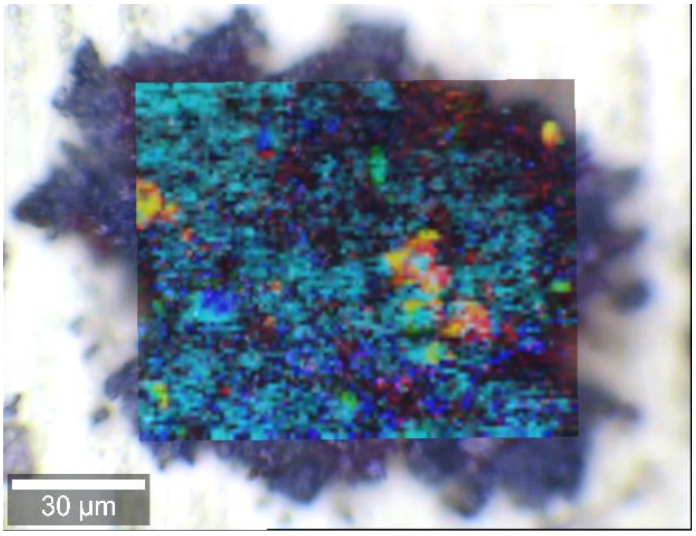

Figure C: Raman mapping for olivine (dark blue), iron oxide (cyan), pyroxene (red) and organics (green) on the Allende sample. The x50 objective was used to perform this measurement.

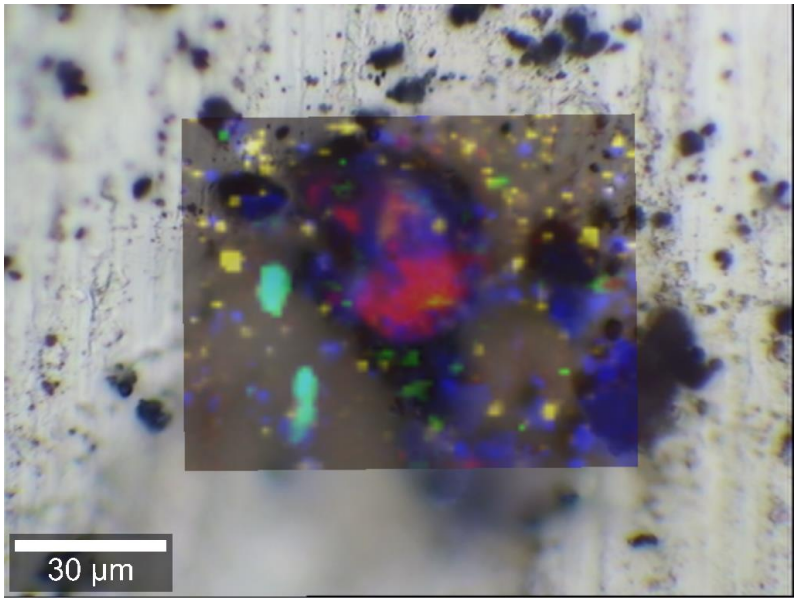

Figure D: Raman mapping for olivine (red), iron oxide (dark blue), pyroxene (green) and organics (yellow) on the Murchison sample. The x50 objective was used to perform this measurement.

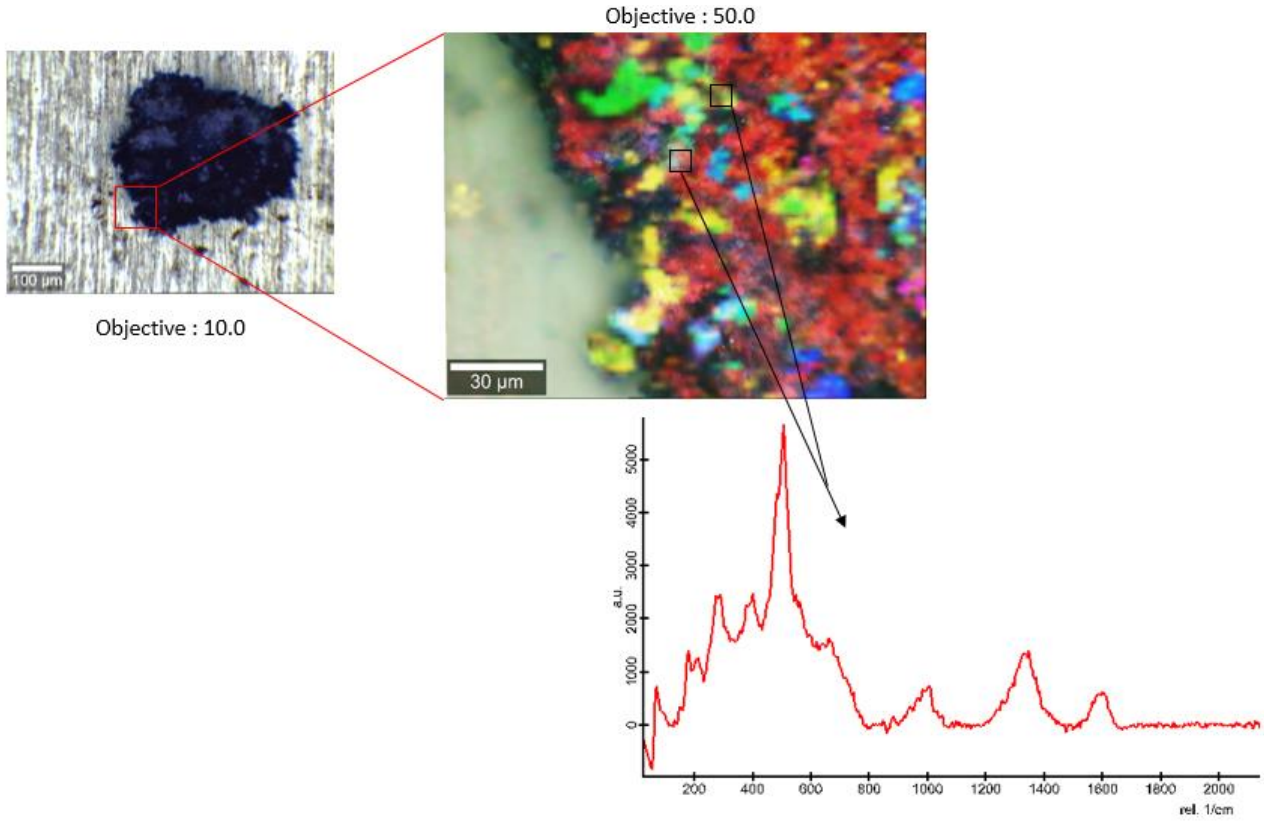

Figure E: Overview of the Raman measurements. Top left: optical picture of the Lance meteorite taken with the x10 objective. Top Right: Raman mapping for olivine (blue), iron oxide (red), pyroxene (yellow) and organics (green) superimposed on the optical picture of the meteorite taken with the x50 objective. Bottom right: Raman spectra of the unknown inclusion and its position on the Raman mapping (black arrow).

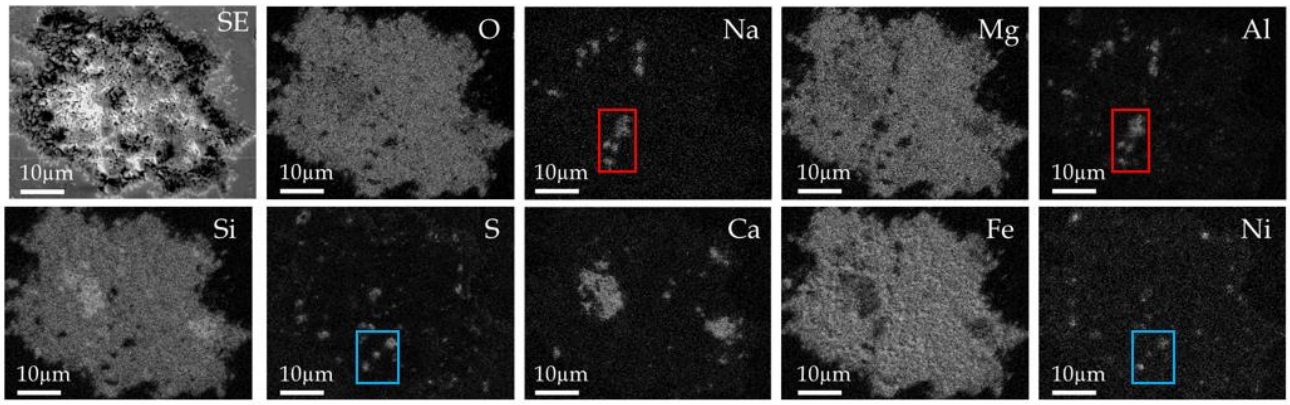

Figure F: SEM-EDX mapping of nine different elements. The Na, Al rich region is marked with a red square and the Ni, S rich region is marked with a blue square.

Band position (cm^{-1})	Assignment	Spectra in which the band is observed	Mineral or chemical function

~ 3670	O-H stretching	7; 8	Alcohol
~ 3660	O-H stretching	7; 13; 15; 24; 27; 28; 29; 30	Phyllosilicate
3650 - 3000	O-H stretching	All	absorbed water
~ 3620	??	13; 15; 29; 30	??
~ 3610	O-H stretching	8; 24	Alcohol
~ 3570	Al-Fe^{2+}-OH stretching	8; 13; 15	Phyllosilicate
~ 3560	??	27; 28	??
~ 3550	Fe^{3+}-Fe^{3+}-OH stretching Fe^{3+}-Fe^{2+}-OH stretching	7; 9; 13; 24	Phyllosilicate
~ 3470	N-H stretching	7; 8; 15; 24; 28; 29; 30	Amine/ amide
~ 3410	N-H stretching	7; 9	Amine/ amide
~ 3370	C≡C stretching	7; 9; 28	Hydrocarbon
~ 3350	C≡C stretching	7; 9; 13; 24; 28; 29	Hydrocarbon
~ 3300	C-H stretching	9; 29	Hydrocarbon
~ 3260	C-H stretching (alkyne)	8; 9; 13; 27; 28; 29; 30	Hydrocarbon
~ 3170	??	13; 27; 30	??
3000 - 2850	??	9	??
2990-2790	N-H stretching (amine salt)	15	Amide/ amine
~ 2960	CH_3 asymmetric stretching	13	Hydrocarbon
~ 2930	CH_2 asymmetric stretching	7; 8; 13; 15; 24; 27; 28	Hydrocarbon
~ 2850	CH_3 asymmetric stretching	7; 13; 27; 28	Hydrocarbon
2800 - 2440	??	8	??
~ 2780	C-H stretching	9; 29	Hydrocarbon
~ 2750	O-H stretching	7; 8; 13; 24; 27; 28	Carboxylic acid
~ 2640	C-H stretching	7; 9	Hydrocarbon
~ 2550	??	8; 9; 28; 29; 30	??
~ 2460		7; 9; 13; 15; 27; 28	??
~ 2340	CO_2 stretching	All	Air contamination
~ 2330	C-O stretching	13	Co_{atm}
~ 2150	C≡C stretching	7; 9; 13; 15; 27; 28; 30	Hydrocarbon
~ 2000	C=C=C (allene)	7; 13; 15; 29	Hydrocarbon
~ 2000	??	15; 24; 28	Carbonate
~ 1940	C-O stretching	8; 9; 13; 24; 27; 28; 29; 30	??
~ 1850	??	8; 27	??
~ 1800	??	13; 15; 28; 30	Carbonate
~ 1790	??	7; 13; 29	??
~ 1730	C=O stretching	9; 13; 24; 27; 28; 30	ketone
~ 1670	C=O stretching	8; 9; 24; 27; 28; 30	Amide/ amine
~ 1630	C=C stretching	7; 13; 15; 24; 27; 28; 29; 30	Hydrocarbon
~ 1540	N-H bending (amine)	15	Amide/ amine
~1520	N-O stretching	9; 30	Amide/ amine
~ 1480	CH_2 scissors	15; 30	Hydrocarbon
~ 1450	??	7; 8; 9; 13; 15; 24; 27; 28; 29; 30	Carbonate
~ 1440	??	7	??
~ 1350	CO_2^-	8; 13	carboxylic acid
Band position (cm^{-1})	**Assignment**	**Spectra in which the band is observed**	**Mineral or chemical function**

~ 1330	C-N stretching	24; 27	Amide/ amine
~ 1300	C=O stretching	7; 8; 13; 15; 27; 28; 30	ketone
~ 1260	C-O-C stretching	7; 8; 9; 24; 27; 30	??
~ 1220	C-O stretching	13	carboxylic acid
~ 1100	Si-O stretching	All	Phyllosilicate
~ 1070	Si-O stretching	13; 14	Phyllosilicate
~ 1010	??	24; 27; 28; 29; 30	Pyroxene
~ 950	N-H bending	7; 8; 9; 14	Amide/ amine
~ 950	??	7; 8; 9; 14	olivine
~ 950	??	24	Pyroxene
~ 950	Si-O stretching	13; 24; 29	Phyllosilicate
~ 880	??	15	olivine
~ 880	??	14; 28	Carbonate
~ 870	??	24; 27; 28; 29	Pyroxene
~ 850	??	29	Carbonate
~ 800	Fe^{3+}-Mg-OH bending Fe^{3+}-Fe^{2+}-OH bending	13; 14	Phyllosilicate
~ 740	Al-O-Si bending	13; 14	Phyllosilicate
~ 715	??	13; 15	Carbonate
~ 680	??	All	Pyroxene
~ 640	??	24; 27; 28	Pyroxene
~ 620	??	All	Pyroxene

Table A: recap chart of every peak assignment

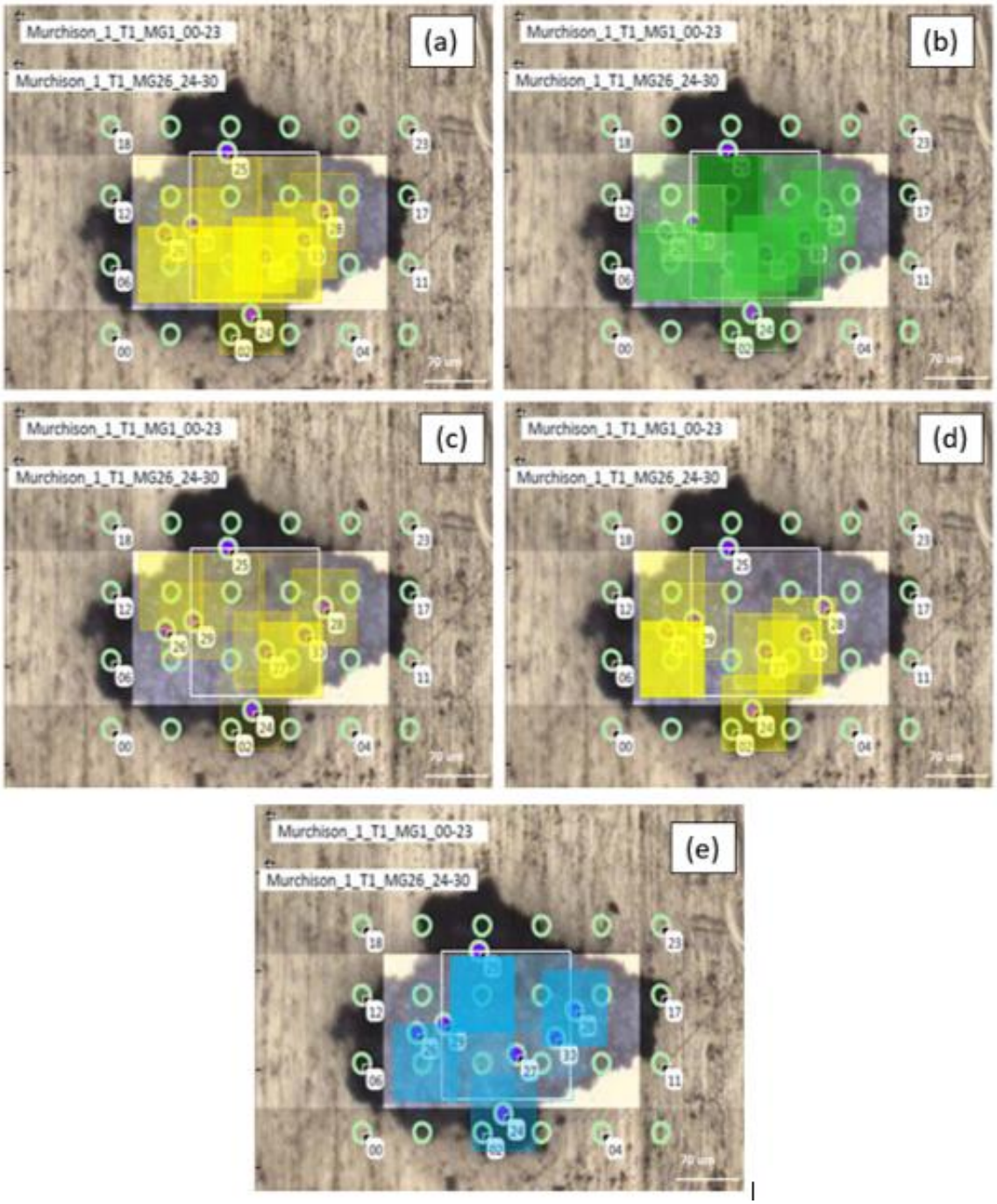

Figure G: Infrared mapping of (a) sulfate mineral, (b) carbonate mineral, (c) C=O stretching for an amide group, (d) C=O stretching for an ester or carboxylic acid group and (e) C=O stretching for a carbonyl group. The shape and the size of the colored squares is the representation of the measurement spot (70µm×70µm).

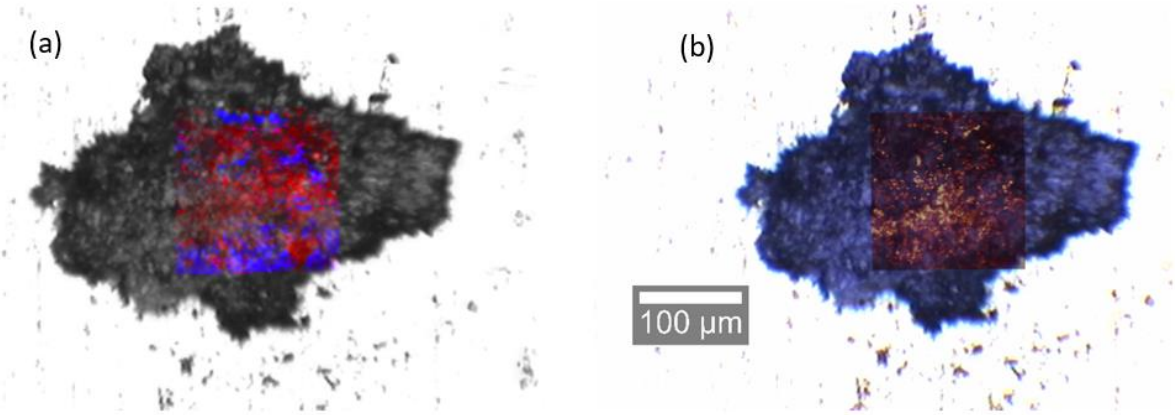

Figure H: Raman mappings of (a) pyroxene in blue (Stenzel et al., 2017) and (b) organics